

1 **Measurement Report: Cloud condensation nuclei (CCN)**  
2 **activity in the South China Sea from shipborne**  
3 **observations during summer and winter of 2021: seasonal**  
4 **variation and anthropogenic influence.**

5 Hengjia Ou<sup>1</sup>, Mingfu Cai<sup>2\*</sup>, Yongyun Zhang<sup>1</sup>, Xue Ni<sup>1</sup>, Baoling Liang<sup>3</sup>, Qibin Sun<sup>4,5</sup>,  
6 Shixin Mai<sup>1</sup>, Cuizhi Sun<sup>6</sup>, Shengzhen Zhou<sup>1</sup>, Haichao Wang<sup>1</sup>, Jiaren Sun<sup>2</sup>, Jun Zhao<sup>1\*</sup>

7 <sup>1</sup>School of Atmospheric Sciences, Guangdong Province Key Laboratory for Climate Change and Natural  
8 Disaster Studies, Southern Marine Science and Engineering Guangdong Laboratory (Zhuhai), Sun Yat-  
9 sen University, Zhuhai, Guangdong 519082, China

10 <sup>2</sup>Guangdong Province Engineering Laboratory for Air Pollution Control, Guangdong Provincial Key  
11 Laboratory of Water and Air Pollution Control, South China Institute of Environmental Sciences, MEE,  
12 Guangzhou 510655, China

13 <sup>3</sup>Guangzhou Sub-branch of Guangdong Ecological and Environmental Monitoring Center, Guangzhou  
14 510006, China

15 <sup>4</sup>Dongguan Meteorological Bureau, Dongguan, Guangdong, 523086, China

16 <sup>5</sup>Dongguan Engineering Technology Research Center of Urban Eco-Environmental Meteorology,  
17 Dongguan, Guangdong, 523086, China

18 <sup>6</sup>Southern Marine Science and Engineering Guangdong Laboratory (Zhuhai), Zhuhai, Guangdong  
19 519082, China

20  
21 *Correspondence:* Mingfu Cai (caimingfu@scies.org) and Jun Zhao (zhaojun23@mail.sysu.edu.cn)

22

23 **Abstract**

24 Understanding seasonal variations in cloud condensation nuclei (CCN) activity and the impact of  
25 anthropogenic emissions in marine environments is crucial for assessing climate change. This study  
26 presents findings from two shipborne observations conducted in the South China Sea (SCS) during the  
27 summer and winter of 2021. In summer, higher particle number concentrations but lower mass  
28 concentrations of non-refractory submicron particles (NR-PM<sub>1</sub>) were observed, driven by Aitken mode  
29 particle dominance. In contrast, winter showed a more balanced distribution between Aitken and  
30 Accumulation mode particles. Summer particles were more hygroscopic, exhibiting higher activation  
31 ratios (ARs) at all supersaturation (SS) levels. Distinct air mass periods were identified: in summer,  
32 terrestrial air masses from Luzon ("Luzon" period), the Indochinese Peninsula ("Indochinese Peninsula"  
33 period), and marine air masses; in winter, periods were influenced by Mainland China ("Mainland China"  
34 period), a mix of Mainland China and marine air masses ("Mixed" period), and purely marine air masses.  
35 The "Luzon" period in summer exhibited the highest particle number concentration, especially in the  
36 Aitken mode, resulting in the highest CCN number concentration (N<sub>CCN</sub>). Aerosol hygroscopicity was  
37 higher during the "Indochinese Peninsula" period compared to the "Luzon" period, leading to a higher  
38 bulk AR due to the combination of higher hygroscopicity and a greater fraction of accumulation mode  
39 particles. The "Mainland China" period in winter showed a high nitrate fraction in the NR-PM<sub>1</sub>, but the  
40 inorganic fraction was similar to it in "Luzon" period, resulting in comparable hygroscopicity at low SS  
41 to the "Luzon" period. However, smaller particle hygroscopicity was significantly lower in the  
42 "Mainland China" period compared to summer. The "Mixed" period in winter exhibited a higher fraction  
43 of accumulation mode particles, causing a higher bulk AR compared to the "Mainland China" period.  
44 Overall, summer terrestrial air masses increased ~~the Aitken mode~~ particle and CCN concentration, while  
45 winter terrestrial air masses led to higher concentration of large ~~particles~~ and lower hygroscopicity of  
46 fine ~~particles~~. CCN closure analysis, considering aerosol composition and mixing state, revealed that  
47 summer ~~aerosols were~~ primarily internally mixed, whereas smaller aerosols in winter ~~were primarily~~  
48 externally mixed. The potential effect of undetected sea salt may lead to an underestimation of aerosol  
49 hygroscopicity in summer. This study highlights significant seasonal differences in aerosol properties  
50 and the impact of different types of terrestrial air masses on CCN activity in the SCS, contributing to our  
51 understanding of regional climate influences.

Deleted: Aitken

Deleted: particle

Deleted: particle

Deleted: aerosol was

Deleted: was

57 **1.Introduction**

58 Aerosols can act as cloud condensation nuclei (CCN), influencing cloud formation, lifespan, and  
59 albedo, thus indirectly impacting global radiative balance (Fletcher et al., 2011; Albrecht, 1989). The  
60 aerosol-cloud interaction currently represents the largest uncertainty in radiative forcing within climate  
61 models, ranging from -1.7 to -0.3 W m<sup>-2</sup> (IPCC, 2021). This uncertainty can be [partially](#) attributed to the  
62 significant spatiotemporal variability in the aerosol size distribution and the ability of atmospheric  
63 aerosol particles acting as CCN (CCN activity) (Fitzgerald, 1973; [Jimenez et al., 2009](#); [Sihto et al., 2011](#)).  
64 Thus, field measurements of aerosol size distribution and physicochemical properties are needed to better  
65 understand the radiative forcing exerted by atmospheric aerosol particles.

Deleted: (Jimenez et al., 2009)

Deleted: (Sihto et al., 2011)

66 Previous studies suggest that particle number size distribution (PNSD) is a primary factor  
67 influencing CCN concentrations (Dusek et al., 2006; Rose et al., 2010; Pöhlker et al., 2016; Burkart et  
68 al., 2011). The PNSD can account for 84–96% of the variability in the CCN concentrations ( $N_{CCN}$ ) (Dusek  
69 et al., 2006), while CCN activities may also play a significant role in the  $N_{CCN}$  (Quinn et al., 2008; Cai  
70 et al., 2018; Ovadnevaite et al., 2017; Liu et al., 2018; Crosbie et al., 2015), which are primarily governed  
71 by the particle size, chemical composition, mixing state, surface tension, and hygroscopicity (Köhler,  
72 1936; Seinfeld and Pandis, 2016). Among these factors, the impact of hygroscopicity on CCN activities  
73 has received great attention in recent years (Petters and Kreidenweis, 2007; Ajith et al., 2022; Rose et al.,  
74 2010). Petters and Kreidenweis (2007) proposed the  $\kappa$ - Köhler theory based on the Köhler theory to  
75 quantify the ability of aerosol particles to absorb moisture and become CCN based on the aerosol  
76 hygroscopicity parameters ( $\kappa$ ). Ajith et al. (2022) showed that 64% of particles can be activated as CCN  
77 when  $\kappa$  is equal to 0.37, whereas when  $\kappa$  decreases to 0.23, only 48% of particles can be activated in the  
78 tropical coastal area.

79 Significant seasonal variations in PNSD and hygroscopicity under both terrestrial and marine  
80 environments were observed in previous field observations, leading to the seasonal variations in  $N_{CCN}$   
81 (Crosbie et al., 2015; Schmale et al., 2018; Burkart et al., 2011; Bougiatioti et al., 2009; Sihto et al., 2011;  
82 Leena et al., 2016; Ross et al., 2003; Gras and Keywood, 2017; Quinn et al., 2019). Crosbie et al. (2015)  
83 revealed that in the urban area of Arizona particles had larger sizes, higher hygroscopicity, and  $N_{CCN}$  was  
84 also higher during winter, while a higher abundance of smaller particles was observed during summer  
85 owing to stronger photochemical reactions. In pristine environments like mountain, coastal, and forested

88 regions, seasonal variations in  $N_{CCN}$  and PNSD were more pronounced than urban and rural areas  
89 (Schmale et al., 2018). Pöhlker et al. (2016) observed significant differences in  $N_{CCN}$  between the wet  
90 and dry seasons in the Amazon rainforest, while the  $\kappa$  values remained relatively stable. They also noted  
91 increased particle concentrations and aerosol hygroscopicity, both subject to the impact of long-range  
92 transport originating from anthropogenic emissions. Observations in marine areas during different  
93 seasons are relatively scarce compared with those in inland areas. Gras (1995) found that both particle  
94 concentration and  $N_{CCN}$  in the Southern Ocean reached their peaks during summer and gradually decrease  
95 to their valleys in winter. Quinn et al. (2019) showed that sea spray aerosols make a relatively significant  
96 contribution to  $N_{CCN}$  only during winter in the Western North Atlantic, while in other seasons, the primary  
97 contribution comes from biogenic aerosols oxidized from dimethyl sulfide (DMS). Zheng et al. (2020)  
98 revealed that sulfate dominates the particle condensational growth to CCN sizes during summer in the  
99 [Eastern North Atlantic](#), while secondary organic aerosols played a significant role in particle growth  
100 throughout all seasons. These results indicate that CCN activity and concentration could vary in a large  
101 range during different seasons. Thus, further observations across different seasons in marine  
102 environments are needed to enhance our understanding of marine CCN activities and their seasonal  
103 variations.

Deleted: North Atlantic

Deleted:

104 The South China Sea (SCS), located in Southeast Asia and bordered by China, the Indochinese  
105 Peninsula, and Maritime Southeast Asia, is significantly influenced by air pollutants transported through  
106 terrestrial air masses. Studies have shown that these pollutants play a crucial role in determining aerosol  
107 concentration and properties in the region (Atwood et al., 2017; Xiao et al., 2017; Geng et al., 2019;  
108 Liang et al., 2021; Sun et al., 2023; Qin et al., 2024). For instance, Xiao et al. (2017) reported that 69.7%  
109 of nitrate and 57.5% of sulfate in the SCS originated from fossil fuel combustion, particularly coal  
110 burning in Chinese coastal regions. Additionally, Liang et al. (2021) and Sun et al. (2023) observed an  
111 increase in the organic fraction and concentration of submicron aerosols when the region was influenced  
112 by terrestrial air masses from Mainland China and the Indochinese Peninsula in the northern SCS. Further  
113 studies highlighted the variation in aerosol properties under different air mass influences. Atwood et al.  
114 (2017) found a significant bimodal particle distribution with a  $\kappa$  value of 0.65 in the southern SCS under  
115 marine air mass influence, whereas a unimodal distribution with a  $\kappa$  of 0.4 was observed under  
116 continental air mass influence.

119 The SCS experiences a typical monsoon climate with distinct seasonal wind direction changes  
120 (Wang et al., 2009). The northeast monsoon, occurring from November to March, is characterized by  
121 stronger average wind speeds and longer period compared to the southwest monsoon, which dominates  
122 from June to August. The transitional periods occur from April to May and September to October. During  
123 the northeast monsoon, air pollutants are primarily transported to the SCS by terrestrial air masses from  
124 China (Xiao et al., 2017; Liu et al., 2014; Geng et al., 2019). In contrast, during the summer, pollutants  
125 mainly originate from terrestrial air masses from the Indochinese Peninsula and Maritime Southeast Asia  
126 (Geng et al., 2019; Liang et al., 2021; Sun et al., 2023). These varying sources of anthropogenic emissions  
127 exert different impacts on CCN activity differently across seasons. Additionally, when the marine  
128 boundary layer over the SCS is influenced by various natural and anthropogenic sources, resulting in  
129 altered aerosol properties, the characteristics of cumulus clouds are correspondingly affected (Miller et  
130 al., 2023). This indicates that aerosol-cloud interactions vary between winter and summer seasons.  
131 However, due to limited observational data, our understanding of seasonal variations in CCN activity in  
132 the SCS remains incomplete. Conducting comprehensive observational studies on CCN activity across  
133 different seasons is essential for improving our understanding of aerosol-cloud interactions on the SCS.

Deleted: exerts

Deleted: the fraction of high cloud over the SCS varies from approximately 0.3 to 0.7 across different months, indicating that aerosol-cloud interactions in the region may differ between seasons (Lu et al., 2022).

134 In this study, we conducted two shipborne observations in the SCS during summer (May 5–June 9,  
135 2021) and winter (December 19–29, 2021). Our observations with online instruments focused on  
136 measuring aerosol chemical composition, PNSD, and CCN activation in the region. Our results provide  
137 valuable insights into the differences in CCN activity between winter and summer, as well as the  
138 influence of different types of terrestrial air masses on CCN activity in the SCS across different seasons.

## 139 2. Methodology

### 140 2.1 Cruise information and onboard measurements

#### 141 2.1.1 Cruise information

142 This study consists of two research cruises conducted during the summer and winter of 2021,  
143 respectively. These two cruises were interdisciplinary scientific expeditions, integrating fields such as  
144 marine geology, oceanography, and atmospheric environment. The primary objective in atmospheric  
145 environment was to investigate the impact of summer and winter monsoons on the atmospheric  
146 environment of the South China Sea (SCS). The summer and winter cruises were carried out respectively  
147 by the vessels "Tan Kah Kee" and "Sun Yat-sen University". The "Tan Kah Kee" is an oceanographic

153 research vessel with a length of 77.7 meters, a beam of 16.24 meters, and a displacement of 3611 tons.  
154 The "Sun Yat-sen University" is a comprehensive oceanographic training vessel with a total length of  
155 114.3 meters, a beam of 19.4 meters, and a displacement of 6880 tons.

156 The first cruise was from May 5<sup>th</sup> to June 9<sup>th</sup>, 2021. The cruise started from Xiamen Port and  
157 traversed from the northern to the central-southern South China Sea, and then circled back near Hainan  
158 Island, and finally returned to Xiamen Port. The second cruise was from December 19<sup>th</sup> to December  
159 29<sup>th</sup>, 2021. It began from Gaolan Port in Zhuhai and reached the vicinity of Yongxing Island, and  
160 ultimately returned to Gaolan Port (Fig. 1a). Unfortunately, due to adverse weather conditions, such as  
161 strong winter monsoon winds causing poor sea conditions, and the fact that it was the first scientific  
162 deployment of the research vessel Sun Yat-sen University, the winter cruise had a shorter duration and  
163 covered a narrower spatial range, remaining only in the northern SCS (Fig. S1), compared to the summer  
164 cruise. On both cruises, most of the instruments were housed in a single compartment and the sampling  
165 lines were extended from the window of the compartment to the height of the ship's bridge (~17 m above  
166 sea level) (Fig. 1a).

Deleted: 1a

### 167 2.1.2 Size-resolved cloud condensation nuclei activity measurement

168 [The size-resolved CCN activity was measured using the scanning mobility CCN analysis \(SMCA\)](#)  
169 [method proposed by Moore et al. \(2010\), employing a combination of a scanning mobility particle sizer](#)  
170 [\(SMPS\) system and a cloud condensation nuclei counter \(CCNc-200, DMT Inc., USA\) \(Fig. S2\).](#) The  
171 SMPS system consisted of a differential mobility analyzer (DMA; model 3082, TSI., Inc.) and a  
172 condensation particle counter (CPC; model 3756, TSI Inc.). The SMPS and the CCNc system were used  
173 to measure PNSD and size-resolved CCN number concentration at a mobility size range of 10–500 nm  
174 and 10–593 nm in summer and winter campaign, respectively. Unfortunately, due to the malfunction of  
175 flow sensor in the column B [on both cruises](#), only the data from column A is presented in this study.  
176 During the SMCA measurement, the particles were first passed through a Nafion dryer to remove  
177 moisture, then neutralized using a neutralizer. After that, they were subjected to size selection with a  
178 DMA. The particles were then split between a CPC (1 L min<sup>-1</sup>) for particle concentration measurement  
179 and a CCNc (0.5 L min<sup>-1</sup>) for CCN measurement at a specific supersaturation ([SS](#)). To maintain sample  
180 flow through the DMA, dilution air (0.5 L min<sup>-1</sup>) was added to the CPC inlet stream. The effect of the  
181 dilution air was accounted for in the PNSD data processing (Fig. S2). The supersaturation of the CCNc

Deleted: The size-resolved CCN activity was measured with a combination of a scanning mobility particle sizer (SMPS) system and a cloud condensation nuclei counter (model CCNc-200, DMT Inc., USA), the scanning mobility CCN analysis (SMCA) method initially proposed in Moore et al. (2010). ...

Deleted: (SS)

190 was set at 0.2 %, 0.4 %, and 0.7 % in summer campaign and 0.1%, 0.2 %, 0.4 %, and 0.7 % in winter  
191 campaign, respectively. [During the measurement process, each supersaturation level was held constant](#)  
192 [for 20 minutes, with the DMA completing a full scanning cycle every 5 minutes. During the](#)  
193 [measurements, supersaturation levels varied incrementally between 0.1% and 0.2%, 0.2% and 0.4%, and](#)  
194 [0.4% and 0.7%, with temperature stabilization times ranging from a few seconds to several tens of](#)  
195 [seconds. However, reducing the supersaturation from 0.7% to 0.1% or 0.2% required approximately 5](#)  
196 [minutes for stabilization. For data processing, only instances where the temperature remained stable](#)  
197 [throughout the DMA scanning phase were included in the analysis.](#) Before the measurements, the CCNc  
198 was calibrated with ammonium sulfate ((NH<sub>4</sub>)<sub>2</sub>SO<sub>4</sub>) particles at each set SS. Detailed description of the  
199 instrument configuration and calibration can be found in Cai et al. (2018). [The uncertainty in the](#)  
200 [instrument's measurement of size-resolved particle number concentration is approximately 5%-6%](#)  
201 [\(Morre et al. 2010\).](#)

Formatted: Font: (Asian) +Body Asian (等线)

### 202 2.1.3 Aerosol chemical composition measurement

203 The chemical composition of atmospheric non-refractory submicron particulate matter (NR-PM<sub>1</sub>),  
204 including sulfate, nitrate, organics, ammonium, and chloride, was measured using an online time-of-  
205 flight ACSM (ToF-ACSM; Aerodyne Inc., USA). The sampling time of the ToF-ACSM was  
206 approximately 10 min. The [ionization efficiency \(IE\) and](#) relative ionization efficiency (RIE) values of  
207 the instrument were calibrated using ammonium nitrate (NH<sub>4</sub>NO<sub>3</sub>) and ammonium sulfate ((NH<sub>4</sub>)<sub>2</sub>SO<sub>4</sub>)  
208 both before the start and after the completion of the campaigns. [The calibration gives an IE value of](#)  
209 [103.4 ions pg<sup>-1</sup> and 98.9 ions pg<sup>-1</sup> for nitrate in summer and winter cruises, respectively.](#) The RIE values  
210 for ammonium were 3.31 and 3.33 during the summer and winter, respectively, while the ones for sulfate  
211 were 1.02 and 0.81 during the summer and winter, respectively. The collection efficiency (CE) was  
212 determined as shown in Sun et al. (2023) and time-independent CE values were used in this study.  
213 Detailed CE calculation [and discussion](#) can be found in the supplementary (Text S1, and Fig. S3). [The](#)  
214 [values obtained using the time-independent CE method show a deviation of approximately 3% compared](#)  
215 [to those obtained with a constant CE of 0.5. Assuming an average aerosol density of 1.5 g cm<sup>-3</sup> \(Geller](#)  
216 [et al., 2006\), the mass concentrations measured by the SMPS and ToF-ACSM exhibit a strong overall](#)  
217 [correlation, with correlation coefficients of 0.84 in summer and 0.93 in winter. The black carbon \(BC\)](#)  
218 [mass concentrations were measured using an aethalometer \(Model AE33, Magee Scientific, USA\) with](#)

Formatted: Superscript

Formatted: Superscript

Formatted: Superscript

219 a 1-minute time resolution (Drinovec et al., 2015). Notably, the BC mass concentrations obtained from  
220 AE33 are referred to as equivalent BC mass concentrations, as they represent the combined light  
221 absorption of BC at 880 nm. Prior to entering the AE33, the sampled air was passed through a PM<sub>2.5</sub>  
222 cyclone (BGI Inc., Waltham, MA, USA) to exclude particles larger than 2.5 μm.

Formatted: Subscript

Deleted: The black carbon concentrations were measured with an aethalometer (AE33, Magee Scientific).

### 223 2.1.4 Meteorological parameter measurements

Formatted: Heading 3, Indent: First line: 0 cm

224 The meteorological elements, including temperature, relative humidity (RH), wind speed, and wind  
225 direction, were measured by the combined automatic weather station (AWS430, Vaisala Inc., Finland)  
226 onboard the vessels (Sun et al., 2024). During the winter cruises, meteorology data before 12.22 was  
227 missed due to the calibration for the automatic weather station (WXT536, Vaisala Inc., Finland) before  
228 12.22. The timeseries of meteorological data were presented in Fig. S5. The AWS430 provides  
229 measurement accuracies of ±2% for wind speed, ±2% for wind direction, ±0.3°C for temperature, and  
230 ±1% for relative humidity (within the range of 0–90%). Similarly, the WXT536 offers accuracies of ±3%  
231 for wind speed, ±3% for wind direction, ±0.3°C for temperature, and ±3% for relative humidity (within  
232 the range of 0–90%) (www.vaisala.com).

Deleted: S4

Deleted:

## 233 2.2 Data analysis

Formatted: Heading 3, Indent: First line: 0 cm

### 234 2.2.1 CCN activation

235 The size-resolved number concentration of total particle and cloud condensation nuclei were  
236 obtained from the SMPS and CCNc through the SMCA method. The activation diameter was determined  
237 by fitting the activation ratio (AR,  $N_{CCN}/N_{CN}$ ) and dry diameter at each supersaturation through the  
238 following equation:

$$239 \quad AR = \frac{B}{1 + \left(\frac{D_p}{D_{50}}\right)^C}, \quad (1)$$

240 where AR indicates the size-resolved AR,  $D_p$  represents dry particle diameter (nm); B, C, and  $D_{50}$  are the  
241 three fitting parameters, representing the asymptote, the slope, and the inflection point of the sigmoid,  
242 respectively (Moore et al., 2010). The  $D_{50}$  parameter, also known as the critical diameter, corresponds to  
243 the particle size at which 50% of the particles are activated at a specific SS. The fitting results from  
244 SMCA method measured in this study are presented in Fig. S6.

Deleted: S5

245 The hygroscopicity parameter ( $\kappa$ ) which represents CCN activity according to  $\kappa$ -Köhler equation is  
246 calculated as follows (Petters and Kreidenweis, 2007):



$$\kappa = \frac{4A^3}{27D_{50}^3(\ln S_c)^2}, A = \frac{4\sigma_{s/a}M_w}{RT\rho_w} \quad (2)$$

where  $\rho_w$  is the density of pure water (about 997.04 kg m<sup>-3</sup> at 298.15 K),  $M_w$  is the molecular weight of water (0.018 kg mol<sup>-1</sup>),  $\sigma_{s/a}$  corresponds to the surface tension of the solution-air interface and is assumed to be equal to the surface tension of pure water ( $\sigma_{s/a}=0.0728$  N m<sup>-1</sup> at 298.15 K),  $R$  is the universal gas constant (8.314 J mol<sup>-1</sup> K<sup>-1</sup>),  $T$  denotes thermodynamic temperature in kelvin (298.15 K), and  $D_{50}$  is the critical diameter (in m). Additionally, it is noting that the estimated  $\kappa$  values refer to particles with the

$D_{50}$ .  
According to  $\kappa$ -Köhler theory, in the following discussion, the hygroscopicity of small particles is associated with hygroscopicity at high SS, whereas the hygroscopicity of large particles is linked to hygroscopicity at low SS.

During part of the summer measurement period, the  $D_{50}$  at 0.7% supersaturation ranged between 30 and 40. However, due to lower concentrations during these times, instrument noise introduced greater measurement uncertainty, as demonstrated in Fig. S7. Consequently, the average  $D_{50}$  and  $\kappa$  at 0.7% SS are not included in Table 1.

### 2.2.2 Closure Method

According to Petters and Kreidenweis. (2007),  $\kappa$  can be predicted by a simple mixing rule based on chemical volume fractions:

$$\kappa_{sim} = \sum_i \varepsilon_i \kappa_i \quad (3)$$

where  $\varepsilon_i$  and  $\kappa_i$  are the volume fraction and hygroscopicity parameter for the specific dry component in the mixture. We obtained  $\varepsilon$  from aerosol chemical composition measured by the ToF-ACSM. In this study,  $\kappa$  for (NH<sub>4</sub>)<sub>2</sub>SO<sub>4</sub> (0.48), NH<sub>4</sub>NO<sub>3</sub> (0.58), and NaCl (1.1) represent the  $\kappa$  of SO<sub>4</sub><sup>2-</sup>, NO<sub>3</sub><sup>-</sup>, and Cl<sup>-</sup> provided by the ToF-ACSM (Huang et al., 2022). Besides, the  $\kappa$  of organic was 0.1 at this study according to Huang et al. (2022). The density of (NH<sub>4</sub>)<sub>2</sub>SO<sub>4</sub>, NH<sub>4</sub>NO<sub>3</sub>, NaCl and organic are 1769 kg m<sup>-3</sup>, 1720 kg m<sup>-3</sup>, 2165 kg m<sup>-3</sup>, and 1400 kg m<sup>-3</sup> (Huang et al., 2022; Gysel et al., 2007).

### 2.2.3 CCN concentration and activation ratio calculation

Due to the malfunction of the column B, the CCN concentration ( $N_{CCN}$ ) was calculated based on the size-resolved AR at a specific SS from SMCA method and observed particle number concentration. It can be calculated by the following equation (Cai et al., 2018):

Deleted: , which are the smallest particles that can be activated at a given SS

Formatted

Deleted:

Deleted: S6

Formatted

Formatted: No underline, Font color: Auto

284  $N_{CCN}(SS) = \int_0^{\infty} AR(SS, D_p)N_{CN}(D_p)dD_p$  (4)

285 where  $N_{CCN}(SS)$  is the CCN concentration at a specific SS,  $AR(SS, D_p)$  is the ratio of  $N_{CCN}$  at a specific  
 286 SS to  $N_{CN}$  on a specific diameter from the SMCA method and  $N_{CN}(D_p)$  is the particle number  
 287 concentration at a specific diameter ( $D_p$ ). Due to the absence of direct measurements for total  $N_{CCN}$ , we  
 288 refer to the  $N_{CCN}$  derived from Eq. (4) as observed values ( $N_{CCN,obs}$ ) in this study. Previous research has  
 289 shown that this method (size-resolved CCN from one column in CCNc-200) provides results closely  
 290 matching those obtained from direct measurement (from another column in CCNc-200), supporting its  
 291 reliability (Meng et al., 2014; Latham and Nenes, 2011).

292 The  $N_{CCN}$  (referred as  $N_{CCN,sim}(SS)$ ) can be predicted by  $D_{50}$  from closure method ( $D_{50,sim}(SS)$ )  
 293 and  $N_{CN}$  according to following equation (Jurányi et al., 2011):

294  $N_{CCN,sim}(SS) = \int_{D_{50,sim}(SS)}^{\infty} N_{CN}(D_p)dD_p$  (5)

295 where the  $D_{50,sim}(SS)$  is calculated based on the eq. (2) and (3).

296 The bulk AR at a specific SS can be calculated by:

297  $AR(SS) = \frac{N_{CCN,obs}(SS)}{N_{CN,tot}}$  (6)

298 where the  $N_{CN,tot}$  represents the total particle number concentration.

299 To investigate the impact of the fraction and mixing state of aerosol on  $N_{CCN}$ , two CCN simulation  
 300 **schemes** are applied in this study (Patel et al., 2021).

301 (1) Internal-mixed scheme: the aerosol composition from the ToF-ACSM was assumed to be size-  
 302 independent and internally mixed. All **aerosols have** an identical chemical composition in the  
 303 whole size range.  $N_{CCN}$  is calculated by  $\kappa_{sim}$  and measured PNSD according to Eq. (2), Eq. (3),  
 304 and Eq. (5) (Fig. **S8a**).

305 (2) External-mixed scheme: the aerosol composition from the ToF-ACSM was assumed to be size-  
 306 independent and externally mixed. Four **types of aerosols** ((NH<sub>4</sub>)<sub>2</sub>SO<sub>4</sub>, NH<sub>4</sub>NO<sub>3</sub>, NaCl and  
 307 organic) are assumed to have **the same proportion** for all sizes. The  $D_{50}$  from each species was  
 308 calculated **by Eq. (2)** according to their  $\kappa$  values mentioned in 2.2.2.  $N_{CCN}$  is calculated  
 309 according to the Eq. (5) (Fig. **S8b and Table S1**).

310 To access the simulation result from these two schemes, normalized mean bias (NMB) was used in  
 311 this study:

Deleted: scheme

Deleted: aerosol has

Deleted: S7a

Deleted: type

Deleted: aerosol

Deleted: a same proportion

Deleted: S7b

319 
$$NMB = \frac{\sum(N_{CCN,sim} - N_{CCN,obs})}{\sum N_{CCN,obs}} \quad (7)$$

320 where  $N_{CCN,sim}$  is the simulated  $N_{CCN}$  from two schemes, and  $N_{CCN,obs}$  is the observed  $N_{CCN}$ .

321 **2.2.4 Fitting of log-normal modes to particle number size distributions**

322 The multi-lognormal distribution function (Eq. (8)) is used to parameterize and optimize the  
 323 descriptions of the measured PNSD (Heintzenberg, 1994) and is widely applied in aerosol research (Cai  
 324 et al., 2020; Boyer et al., 2023; Zhu and Wang, 2024). An automatic mode-fitting algorithm (Hussein et  
 325 al., 2005) is used to generate the model-fitted results.

326 
$$f(D_p, \bar{D}_{pg,i}, N_i, \sigma_{g,i}) = \sum_{i=1}^n \frac{N_i}{\sqrt{2\pi} \log(\sigma_{g,i})} \times \exp \left[ -\frac{[\log D_p - \log \bar{D}_{pg,i}]^2}{2(\log \sigma_{g,i})^2} \right] \quad (8)$$

327 where  $D_p$  is the diameter of a particle. Each lognormal mode is characterized by three parameters:  
 328 the mode number concentration ( $N_i$ ), geometric variance ( $\sigma_{g,i}$ ), and geometric mean diameter (GMD,  
 329  $\bar{D}_{pg,i}$ ). The total number of lognormal modes used to describe the PNSD is denoted by  $n$ . These modes  
 330 are fitted using an algorithm applied to each particle size distribution, with one to three log-normal  
 331 distributions used per time step. The algorithm classifies the PNSD into nucleation, Aitken, and  
 332 accumulation modes based on their geometric mean diameters (GMDs). The GMD for nucleation modes  
 333 (GMD1) typically ranges from 3 to 30 nm, for Aitken modes (GMD2) from 30 to 100 nm, and for  
 334 accumulation modes (GMD3) above 100 nm (Heintzenberg, 1994; Hussein et al., 2005; Zhu and Wang,  
 335 2024).

336 **2.2.5 Backward trajectory simulation and cluster analysis**

337 Backward trajectory calculations were performed using the MeteoInfo, an open-source software  
 338 (Wang, 2014) to determine potential source origins. Weekly GDAS1 (Global Data Assimilation System  
 339 at a resolution of 1°) files were downloaded from the NOAA Air Resource Laboratory (ARL) website  
 340 (<https://www.ready.noaa.gov/gdas1.php>). The calculation of backward trajectories is performed every  
 341 1 hour based on the location mentioned below, generating 72-hour backward trajectories at 500m.

342 To clarify the sources of air masses, the cluster analysis was applied in this study, which was  
 343 performed by TrajStat, a plug-in module of MeteoInfo, based on k-means method  
 344 ([http://meteothink.org/docs/trajstat/cluster\\_cal.html](http://meteothink.org/docs/trajstat/cluster_cal.html)). According to the report by the China  
 345 Meteorological Administration (Chao et al., 2022), the summer monsoon in 2021 broke out during the

Deleted: 6

Formatted: Indent: First line: 2 ch

Deleted: log

Deleted: exp

Formatted: Subscript

Formatted: 公式1, Justified, Indent: First line: 0.71 cm

Formatted: Subscript

Formatted: Subscript

Formatted: Subscript

Deleted:

Deleted: 4

Formatted: Heading 3, Indent: First line: 0 cm

351 sixth pentad of May. Therefore, based on the timing of the monsoon onset and the actual trajectory of the  
352 ship, we selected two representative midpoints of the ship track for backward trajectory calculations and  
353 cluster analysis in summer: the midpoint of the ship's track before the onset of the summer monsoon  
354 (May 5-23) and the midpoint of the track after the summer monsoon began (May 24-June 9). In the  
355 winter cruise, backward trajectories calculation and cluster analysis were performed at two specific  
356 locations: the ship's anchorage near Big Ten-thousand Mountain Island (December 19-22 and December  
357 27-29) and the midpoint between Dawan Mountain Island and Yongxing Island (December 23-26). To  
358 ensure the accuracy of the backward trajectory calculations and cluster analysis, we compared the  
359 trajectories at the midpoints with those from the ship's actual locations to verify consistency in air mass  
360 sources (Fig. S9). Minor discrepancies may exist between the air mass origins at certain midpoints and  
361 the actual ship locations. However, overall, the air mass origins at the midpoints are representative of  
362 those at the actual locations. We further examined the trajectories for each cluster to verify their alignment  
363 with the air mass origins they represent (Fig. S10). The results demonstrate that cluster analysis was well  
364 conducted. Additionally, figure S10 illustrates the average altitude variation as the age in hours increases  
365 across different periods. During summer, the altitude of the clusters remained below 880 hPa, indicating  
366 that they resided within the boundary layer (about 800 hPa). While in winter, the altitude of the clusters  
367 was higher than in summer, especially for the cluster during the mixed period (peaked at about 755 hPa).  
368 However, these clusters were generally within or close to the boundary layer. These results suggest that  
369 the back trajectories could represent the characteristics of the air masses originating from these specified  
370 regions.

Deleted: was

Deleted: S8

Deleted: S9

Deleted: well-conducted

### 371 2.2.5 Data quality control

372 To ensure reliable atmospheric samples in the SCS and mitigate the influence of research vessel  
373 emissions, we applied the following data processing procedures (Huang et al., 2018; Cai et al., 2020;  
374 Liang et al., 2021).

375 Firstly, we identified organic compounds, black carbon (BC), and small particulate matter (41.4 nm  
376 particles) as indicators of ship emissions, recognizing their sudden peak values as indicative of the ship's  
377 own emissions.

378 Secondly, we accounted for the relative positions of the ship's chimney and the sampling tube.  
379 During the summer cruise, we excluded data corresponding to a relative wind direction (with respect to

384 the ship's bow) between 150° and 270° and a relative wind speed (with respect to the ship's speed) of less  
385 than 2.5 m s<sup>-1</sup> (Fig. S12a, Fig. S13a1, and Fig. S14a-c). During the winter cruise, we excluded data for a  
386 relative wind direction between 150° and 220° and a relative wind speed of less than 2.5 m s<sup>-1</sup> (Fig. S12b,  
387 Fig. S13b1, and Figs. S14d-f).

388 Applying these criteria, 74.8% of the data in summer and 92.2% in winter (both at 10-minute  
389 resolution) were classified as “clean” and retained for analysis. The timeseries of data before and after  
390 quality control is shown in Fig. S15.

### 391 3. Results and discussion

#### 392 3.1 CCN concentration and aerosol characteristics over SCS in summer and winter

393 Figure 2 presented the timeseries of PNSD (a1 and a2), NR-PM<sub>1</sub> mass concentrations and fractions  
394 (b1 and b2, c1 and c2), number concentrations of CCN (d1 and d2), and hygroscopicity κ-values (e1 and  
395 e2) during two campaigns in summer and winter. During the summer cruise, we observed two distinct  
396 periods around the onset of the summer monsoon. The South China Sea (SCS) summer monsoon began  
397 in the sixth pentad of May (Chao et al., 2022). In winter, the influence of the winter monsoon persisted  
398 throughout the entire observation period (Fig. 1c). Despite our measurements being limited to the  
399 northern SCS in winter, the impact of the Northeast Monsoon on the SCS was evident.

400 The average particle number concentration in summer (6966 cm<sup>-3</sup>) was higher than in winter (4988  
401 cm<sup>-3</sup>), primarily due to the higher number concentration of Aitken-mode particles in summer (Fig. 3a-b).  
402 In summer, particles were concentrated in smaller sizes, whereas in winter, particle size distribution was  
403 relatively balanced between the Aitken mode (2185 cm<sup>-3</sup>) and the accumulation mode (2176 cm<sup>-3</sup>) (Fig.  
404 3a-b).

405 The average mass concentration of NR-PM<sub>1</sub> was 3.76 μg m<sup>-3</sup> in summer and increased to 9.39 μg  
406 m<sup>-3</sup> in winter (Fig. 3c-d). In summer, the dominant aerosol component was sulfate (45.5%), followed by  
407 organics (35.8%), ammonium (12.9%), nitrate (4.0%), and chloride (1.9%) (Fig. 3c), similar to the  
408 pattern observed in the northern SCS during the summer of 2018 (Fig. 3e) (Liang et al., 2021). However,  
409 in winter, organics became the predominant aerosol component (37%), with nitrate (22.2%) replacing  
410 sulfate (18.9%) as the highest proportion of inorganic components (Fig. 3d). Although N<sub>CN</sub> was higher  
411 in summer than in winter, the particle volume size distribution indicates that a higher fraction of particles

Deleted: S11a

Deleted: S12a1

Deleted: S13a

Deleted: S11b

Deleted: S12b1

Deleted: S13d

Deleted: S14

Deleted: were

420 was concentrated in larger size in winter, which significantly influenced mass concentration, resulting in  
421 a higher NR-PM<sub>1</sub> concentration (Fig. S16).

Deleted: S15

422 The average number concentration of cloud condensation nuclei ( $N_{CCN}$ ) in summer was higher than  
423 in winter at all supersaturation (SS) levels (Table 1). The ratio of  $N_{CCN}$  between summer and winter was  
424 smaller at high SS ( $N_{CCN, winter}/N_{CCN, summer} = 0.51$  and  $0.54$  at  $0.4\%$  SS and  $0.7\%$  SS, respectively)  
425 compared to low SS ( $N_{CCN, winter}/N_{CCN, summer} = 0.62$  at  $0.2\%$  SS), likely due to the significant difference in  
426 number concentration of Aitken-mode particles between the two seasons (Fig. 3a-b). Compared to the  
427 observation in the Yellow Sea, a region similarly influenced by terrestrial air masses from mainland  
428 China, the  $N_{CCN}$  were lower in winter, while in summer, the  $N_{CCN}$  were more comparable to those  
429 observed in the Yellow Sea ( $4821 \text{ cm}^{-3}$  at  $0.63\%$  SS) (Park et al., 2018).

430 The aerosol hygroscopicity ( $\kappa$ ) was higher in summer than that in winter (Table 1). Besides, the  
431 hygroscopicity pattern varied between seasons: in summer,  $\kappa$  increased with SS (from  $0.47$  to  $0.54$   
432 between  $0.2\%$  SS and  $0.4\%$  SS), while in winter,  $\kappa$  decreased with SS (from  $0.50$  to  $0.15$  between  $0.1\%$   
433 SS and  $0.7\%$  SS) (Fig. 3a-b). [This contrasting trend may be related to the reduced sulfate fraction in  
434 smaller sizes during winter, as sulfate production via DMS oxidation is diminished due to lower sea  
435 surface temperatures in winter \( \$18.0^\circ\text{C}\$ \) compared to summer \( \$29.3^\circ\text{C}\$ \), which in turn inhibits DMS  
436 production by phytoplankton \(Bates et al., 1987; Kouvarakis and Mihalopoulos, 2002\). Additionally, it  
437 could be linked to the mixing state of the particles, with further discussion provided in the following  
438 sections.](#) The winter  $\kappa$  pattern was similar to observations in the Western North Pacific (Table 1) (Kawana  
439 et al., 2020). Additionally, the winter  $\kappa$  values were comparable to those in Guangzhou (Cai et al., 2020),  
440 adjacent to the SCS, indicating that the northern SCS is influenced by air masses from Mainland China  
441 under the significant influence of the Northeast Monsoon during winter.

### 442 3.2 Anthropogenic influence on CCN concentration in different seasons

Deleted: season

443 Cluster analysis revealed distinct periods influenced by various air masses. In summer, three  
444 terrestrial air mass sources were identified: Luzon Island (referred to as “Luzon”), Palawan Island, and  
445 the Indochinese Peninsula, along with a marine air mass source (Fig. 4a). Given the limited influence of  
446 air masses from Palawan Island, this period was excluded from the study. Consequently, the study  
447 focused on periods dominated by air masses from Luzon (“Luzon” period), the Indochinese Peninsula  
448 (“Indochinese Peninsula” period), and marine sources (“Marine-s” period). In winter, the air mass

451 sources included Mainland China, a mixture of Mainland China and the South China Sea (referred to as  
452 “Mixed”), and a marine source (Fig. 4b). These were classified as the “Mainland China” period, “Mixed”  
453 period, and “Marine-w” period, respectively.

454 As shown in figure 5, terrestrial air masses could significantly affect the aerosol chemical  
455 composition in the SCS, resulting in higher NR-PM<sub>1</sub> mass concentration and a higher fraction of organic  
456 compounds compared to those influenced by marine air masses. Additionally, the particles number  
457 concentration in the accumulation mode and the  $N_{CCN}$  at low supersaturation (SS) were higher during  
458 periods influenced by terrestrial air masses (“Luzon” period) than those during marine air mass periods  
459 (Table 2). Notably, we were able to obtain an accurate  $D_{50}$  at 0.7% supersaturation only during the “Luzon”  
460 period in summer. Due to the relatively lower hygroscopicity compared to other summer periods, the  
461 corresponding  $D_{50}$  at 0.7% SS ranged between 40 and 60 nm, with relatively high concentration of CN  
462 and CCN (Fig. S7), allowing for a more precise measurement of  $D_{50}$ . As a result, the  $\kappa$  at 0.7% SS shown  
463 in Fig. 7 was specific to the Luzon period in summer.

464 In summer, the “Luzon” period exhibited the highest  $N_{CN}$ , attributed to the elevated particle  
465 concentration in the Aitken mode, compared to all other periods in both summer and winter (Fig. 6a and  
466 Table 1). This high fraction of Aitken mode particles led to the lowest bulk AR among the summer  
467 periods (Fig. 7a), as a larger fraction of particles centered on a size range lower than the  $D_{50}$  (Fig. 7b).  
468 Furthermore, the prevalence of a higher fraction of Aitken mode particles during terrestrial air mass  
469 periods is commonly correlated with the influence of fresh anthropogenic emissions (Beddows et al.,  
470 2015), which could lower the hygroscopicity and consequently suppress the bulk AR.

471 In the “Indochinese Peninsula” period, the  $N_{CN}$  was lower than it in the “Marine-s” period (Table  
472 2). This difference was mainly due to the variation of Aitken mode particles, while accumulation mode  
473 particles were higher during the “Indochinese Peninsula” period than in “Marine-s” period (Table 2). The  
474 “Marine-s” period primarily occurred during the transition phase before the onset of summer monsoon,  
475 when wind direction shifted from east (Luzon Island direction) to southwest (Indochinese Peninsula  
476 direction). Anthropogenic emissions from Luzon Island still affected the marine atmosphere, leading to  
477 higher concentrations of Aitken mode particles compared to the “Indochinese Peninsula” period (Table  
478 2). The higher fraction of accumulation mode particles and higher hygroscopicity during the  
479 “Indochinese Peninsula” period resulted in a higher bulk AR compared to the “Luzon” period. Despite a  
480 higher organic fraction in NR-PM<sub>1</sub> during the “Indochinese Peninsula” period (Fig. 5), hygroscopicity

Deleted: S6

482 was still higher due to a higher oxidation degree of organics, indicated by a higher m/z 44 to 43 ratio  
483 (5.87 compared to 5.60 in the “Luzon” period) (Lambe et al., 2011; Jimenez et al., 2009). Additionally,  
484 higher wind speeds during this period (7.26 m s<sup>-1</sup> compared to 3.18 m s<sup>-1</sup> in the “Luzon” period)  
485 [potentially led](#) a higher fraction of sea salt (Huang et al., 2022), resulting a higher aerosol hygroscopicity.  
486 Unfortunately, owing to instrument limit, sea salt cannot be detected by the ToF-ACSM.

Deleted: leaded

487 In winter, nitrate accounted for the highest fraction of NR-PM<sub>1</sub> (25.4%) during the “Mainland  
488 China” period compared to other periods (Fig. 5d). Due to similar hygroscopicity between nitrate and  
489 sulfate, as well as comparable inorganic fractions between the “Mainland China” and “Luzon” periods,  
490  $\kappa$  at 0.2% SS was also similar between these two periods (0.30 and 0.33, respectively) (Fig. 7b). However,  
491 aerosol hygroscopicity at small sizes ([high SS](#)) was much lower in the “Mainland China” period than in  
492 the “Luzon” period (Fig. 7b), contributing to the low bulk AR in the “Mainland China” period (Fig. 7a).  
493 The BC mass concentration was higher during the “Mainland China” period (2.25  $\mu\text{g m}^{-3}$ ) compared to  
494 the “Luzon” period (0.72  $\mu\text{g m}^{-3}$ ). This suggests that the lower hygroscopicity in smaller particles ([related  
495 to high SS](#)) during the “Mainland China” period may be attributed to a larger fraction of hydrophobic  
496 BC. [Additionally, as discussed in Section 3.1, the reduced biological activity during winter, which results  
497 in a decline in the fraction of small-particle sulfate and an increase in the fraction of organics, may also  
498 contribute to this low hygroscopicity in small particles, \(at high SS, fig 7b\).](#) The similar fractions of Aitken  
499 mode and accumulation particles indicated that PNSD could not fully explain the low bulk AR in the  
500 “Mainland China” period. Overall, lower N<sub>CN</sub> and bulk AR in the “Mainland China” period compared to  
501 the “Luzon” period resulted in a lower N<sub>CCN</sub>.

Deleted: .

Deleted: Additionally, hygroscopicity at smaller sizes was consistently lower across all winter periods, including the “Mainland China” period, compared to summer. This phenomenon may be related to the reduced sulfate fraction in smaller sizes during winter, as sulfate production via DMS oxidation is diminished due to lower sea surface temperatures in winter (18.0°C) compared to summer (29.3°C), which in turn inhibits DMS production by phytoplankton (Bates et al., 1987).

502 During the “Mixed” period, N<sub>CCN</sub> was lower than in the “Mainland China” period, which can be  
503 attributed to the decreased N<sub>CN</sub> (Table 2). However, accumulation mode particles dominated, unlike in  
504 other terrestrial air mass periods (Fig. 6), resulting in a significantly higher bulk AR compared to the  
505 “Mainland China” period. Organic aerosol hygroscopicity was also higher during the “Mixed” period,  
506 supported by a higher m/z 44 to 43 ratio (3.88 vs. 3.10 in the “Mainland China” period), which explains  
507 the greater hygroscopicity despite a higher organic fraction in NR-PM<sub>1</sub>. Additionally, the lower BC  
508 concentration in the “Mixed” period (1.20  $\mu\text{g m}^{-3}$  vs. 2.25  $\mu\text{g m}^{-3}$  in the “Mainland China” period)  
509 suggests a smaller BC fraction. Moreover, the higher wind speeds during the “Mixed” period (10.77 m



521  $s^{-1}$  vs.  $7.14 m s^{-1}$  in the “Mainland China” period) could have increased the sea salt fraction, further  
522 enhancing aerosol hygroscopicity.

### 523 3.3 CCN closure analysis

524 [The CCN closure method is a widely used approach that connects CCN activity with aerosol](#)  
525 [chemical composition \(Cai et al., 2018; Meng et al., 2014; Deng et al., 2013\). Studies have demonstrated](#)  
526 [that the aerosol mixing state is crucial for accurately parameterizing CCN activity \(Su et al., 2010; Wang](#)  
527 [et al., 2010; Ervens et al., 2010\). Moreover, the CCN closure method provides a framework for](#)  
528 [investigating the influence of aerosol mixing states on CCN activity \(Padró et al., 2012; Wang et al.,](#)  
529 [2018; Patel et al., 2021\).](#) In this study, we applied two schemes based on the CCN closure method, as  
530 described in Section 2.2.3, which consider aerosol composition and mixing state. The fitting parameters  
531 and coefficient of determination ( $R^2$ ) are presented in Table 3, while the fitting plots for both schemes  
532 are shown in Figures [S17](#) and [S18](#). Besides, the NMB from these schemes was presented in Fig. 8.

533 In summer, the NMB was always lower than 0, which indicated that simulated aerosol  
534 hygroscopicity was lower than observed value (Fig. 8). Sea salt which cannot be detected by the ToF-  
535 ACSM may account for higher fraction in summer due to low aerosol concentration in summer (Fig. 3c),  
536 resulting in the underestimation of aerosol hygroscopicity. The NMB exhibits similar trends with changes  
537 in SS in all three periods in summer. Better fitting result appeared at high SS, which indicated a greater  
538 underestimation of the hygroscopicity of larger particles. Besides, “Internal-mixed” scheme had more  
539 precious result than it in “External-mixed” scheme in summer (Fig. 8), suggesting the aerosol was  
540 primary internally mixed in summer.

541 In winter, the “External-mixed” scheme always showed a better result than “Internal-mixed” scheme  
542 at high SS (0.4% SS and 0.7% SS), indicating that particles in small size were mainly externally mixed.  
543 Considering the low hygroscopicity of small-sized particles in winter, it is likely that a significant fraction  
544 of these particles consists of externally mixed BC, which probably originated from fresh anthropogenic  
545 emissions and remains unmixed with other inorganic salts and organics. As BC ages, inorganic and  
546 organic components adhere to it, which would lead to the increase of diameter and particles tended to be  
547 internally mixed (Sarangi et al., 2019). This transition resulted in higher hygroscopicity in large-sized  
548 [particles](#) compared to the smaller-sized particles. Besides, overestimation of aerosol hygroscopicity at  
549 high SS could be owing to a higher fraction of non- or less- hygroscopic component (such as organic and

Deleted: The CCN closure study is widely used to assess the impact of various factors on CCN activity (Patel et al., 2021; Cai et al., 2018; Meng et al., 2014; Deng et al., 2013).

Deleted: S16

Deleted: S17

Deleted: particle

556 BC) at small particle sizes. The predicted  $N_{CCN}$  at 0.1% SS are 20%-40% lower than the observed  
557 concentrations, whereas the predictions at 0.2% SS more closely match the observed values (Fig. 8). This  
558 discrepancy may be due to the higher fraction of sea salt in larger particles. However, due to instrumental  
559 limitations, the ToF-ACSM cannot detect BC and sea salt. Future observations including BC and sea salt  
560 are needed to better assess their effects on aerosol hygroscopicity in the South China Sea (SCS). In  
561 addition, further study of size-resolved aerosol composition can also enhance the understanding on CCN  
562 activity in the SCS.

#### 563 4. Conclusion

564 In this study, we investigated the seasonal variations of cloud condensation nuclei (CCN) activity  
565 in the South China Sea (SCS) and explored the impact of anthropogenic emissions. Shipborne  
566 observations were conducted during the summer (May 5–June 9) and winter (December 19–29) of 2021.  
567 We measured CCN activity, chemical composition, and particle number size distribution (PNSD) using  
568 several onboard instruments, including a ToF-ACSM, a CCNc, an SMPS, and an AE33. Observations  
569 included periods before and after the summer monsoon onset and periods influenced by the winter  
570 monsoon.

571 Our results show that particle number concentration ( $N_{CN}$ ) and CCN number concentration ( $N_{CCN}$ )  
572 were higher in summer than in winter, while the mass concentration of non-refractory submicron  
573 particulate matter (NR- $PM_{10}$ ) was lower in summer. This difference is primarily attributed to the  
574 predominance of Aitken mode particles in summer, contrasted with a higher concentration of  
575 accumulation mode particles in winter. Additionally, aerosol hygroscopicity and bulk AR were found to  
576 be higher in summer than in winter.

577 Backward trajectory and cluster analyses identified distinct influences from various air masses. In  
578 summer, we identified periods affected by terrestrial air masses from Luzon Island (the “Luzon” period)  
579 and the Indochinese Peninsula (the “Indochinese Peninsula” period), alongside a period influenced by  
580 marine air masses (the “Marine-s” period). In winter, the periods were influenced by terrestrial air masses  
581 from Mainland China (the “Mainland China” period), a mix of Mainland China and marine sources (the  
582 “Mixed” period), and marine air masses (the “Marine-w” period). Terrestrial air mass periods exhibited

583 higher NR-PM<sub>1</sub> mass concentrations, organic fractions, and N<sub>CCN</sub>, particularly at low supersaturation,  
584 compared to those influenced by marine air masses.

585 During the “Luzon” period, high N<sub>CCN</sub> was observed, attributed to high N<sub>CN</sub>, especially in the Aitken  
586 mode. This high concentration in the Aitken mode resulted in a low bulk AR at 0.2% SS, indicating a  
587 higher fraction of primary organic aerosol with low hygroscopicity. This caused lower overall  
588 hygroscopicity compared to other summer periods. The lower ratio of m/z 44 to 43 also suggested a  
589 lower oxidation degree of organics in this period. In the "Indochinese Peninsula" period, a higher fraction  
590 of the accumulation mode particles compared to the "Luzon" period led to a higher bulk AR, combined  
591 with increased hygroscopicity.

Deleted: higher

Deleted: compared

592 In winter, the "Mainland China" period was characterized by a high nitrate fraction in the NR-PM<sub>1</sub>.  
593 The similar inorganic fractions in the NR-PM<sub>1</sub> between the “Mainland China” and “Luzon” periods  
594 resulted in comparable aerosol hygroscopicity at low supersaturation (0.2% SS). However, at higher  
595 supersaturation levels (0.4% and 0.7% SS), the “Mainland China” period demonstrated significantly  
596 lower hygroscopicity, which led to a reduced bulk AR at elevated supersaturation. During the "Mixed"  
597 period, accumulation mode particles predominated, leading to a high bulk AR. This indicated an aging  
598 process during transport, with more oxidized organics and higher aerosol hygroscopicity. The lower black  
599 carbon (BC) fraction and the higher sea salt fraction from high wind speed contributed to higher  
600 hygroscopicity in the "Mixed" period compared to the "Mainland China" period, despite the high organic  
601 fraction.

602 The CCN closure analysis, considering aerosol composition and mixing state, revealed that aerosols  
603 in summer were primarily internally mixed, while in winter, small-sized aerosols were primarily  
604 externally mixed. This distinction is crucial for climate models predicting N<sub>CCN</sub> in the SCS. The  
605 underestimation of aerosol hygroscopicity in summer suggests that the effect of sea salt should be  
606 considered.

607 Our study highlights significant seasonal differences in CCN activity in the SCS and the influence of  
608 different types of terrestrial air masses. Future measurements including size-resolved aerosol  
609 composition and obtain more precise measurements of BC and sea salt are needed to better understanding  
610 CCN activity in this region. Additionally, our observation in winter focused on the CCN activity over the  
611 northern SCS, while the influence of air masses from Mainland China in remote SCS was still unclear.

614 Further observations in remote SCS areas could help clarify the anthropogenic influence during winter  
615 under the effect of the winter monsoon.

616

617 *Data availability.* Data from the measurements are available at [https://doi.org/](https://doi.org/10.6084/m9.figshare.25472545)  
618 [10.6084/m9.figshare.25472545](https://doi.org/10.6084/m9.figshare.25472545) (Ou et al., 2024).

619

620 *Supplement.* The supplement related to this article is available online at xxx.

621

622 *Author contributions.* **HO, MC, and JZ** designed the research. **YZ, XN, BL, and CS** performed the  
623 measurements. **HO, MC, QS, and SM** analyzed the data. **SZ and HW** provided useful **comments** on the  
624 paper. **HO, MC, and JZ** wrote the paper with contributions from all co-authors.

625

626 *Competing interests.* The authors declare that they have no conflict of interest.

627

628 *Financial support.* This work was supported by National Natural Science Foundation of China (NSFC)  
629 (Grant No. 42305123 and 42175115) and Basic and Guangzhou Applied Basic Research Foundation  
630 (Grant No. 2023A1515012240 and 2024A1515030221).

631

632 *Acknowledgements.* Additional support from the crew of the vessels "Tan Kah Kee" and "Sun Yat-sen  
633 University" is greatly acknowledged.

634

635

Deleted: comment

637 **Reference**

638 Ajith T. C, Kompalli, S. K., and Babu, S. S.: Role of Aerosol Physicochemical Properties on Aerosol  
639 Hygroscopicity and Cloud Condensation Nuclei Activity in a Tropical Coastal Atmosphere, ACS Earth  
640 Space Chem, 6, 1527-1542, doi:<https://doi.org/10.1021/acsearthspacechem.2c00044>, 2022.

641 Albrecht, B. A.: Aerosols, cloud microphysics, and fractional cloudiness, Science, 245, 1227-1230,  
642 doi:<https://doi.org/10.1126/science.245.4923.1227>, 1989.

643 Atwood, S. A., Reid, J. S., Kreidenweis, S. M., Blake, D. R., Jonsson, H. H., Lagrosas, N. D., Xian,  
644 P., Reid, E. A., Sessions, W. R., and Simpas, J. B.: Size-resolved aerosol and cloud condensation nuclei  
645 (CCN) properties in the remote marine South China Sea - Part 1: Observations and source classification,  
646 Atmos. Chem. Phys., 17, 1105-1123, doi:<https://doi.org/10.5194/acp-17-1105-2017>, 2017.

647 Bates, T. S., Cline, J. D., Gammon, R. H., and Kelly-Hansen, S. R.: Regional and seasonal variations  
648 in the flux of oceanic dimethylsulfide to the atmosphere, J. Geophys. Res. Oceans, 92, 2930-2938,  
649 doi:<https://doi.org/10.1029/JC092iC03p02930>, 1987.

650 Beddows, D. C. S., Harrison, R. M., Green, D. C., and Fuller, G. W.: Receptor modelling of both  
651 particle composition and size distribution from a background site in London, UK, Atmos. Chem. Phys.,  
652 15, 10107-10125, doi:<https://doi.org/10.5194/acp-15-10107-2015>, 2015.

653 Bougiatioti, A., Fountoukis, C., Kalivitis, N., Pandis, S. N., Nenes, A., and Mihalopoulos, N.: Cloud  
654 condensation nuclei measurements in the marine boundary layer of the eastern Mediterranean: CCN  
655 closure and droplet growth kinetics, Atmos. Chem. Phys., 9, 7053-7066, doi:[https://doi.org/10.5194/acp-](https://doi.org/10.5194/acp-9-7053-2009)  
656 [9-7053-2009](https://doi.org/10.5194/acp-9-7053-2009), 2009.

657 [Boyer, M., Aliaga, D., Pernov, J. B., Angot, H., Quéléver, L. L. J., Dada, L., Heutte, B., Dall'Osto,](#)  
658 [M., Beddows, D. C. S., Brasseur, Z., Beck, I., Bucci, S., Duetsch, M., Stohl, A., Laurila, T., Asmi, E.,](#)  
659 [Massling, A., Thomas, D. C., Nøjgaard, J. K., Chan, T., Sharma, S., Tunved, P., Krejci, R., Hansson, H.](#)  
660 [C., Bianchi, F., Lehtipalo, K., Wiedensohler, A., Weinhold, K., Kulmala, M., Petäjä, T., Sipilä, M.,](#)  
661 [Schmale, J., and Jokinen, T.: A full year of aerosol size distribution data from the central Arctic under an](#)  
662 [extreme positive Arctic Oscillation: insights from the Multidisciplinary drifting Observatory for the](#)

663 [Study of Arctic Climate \(MOSAIC\) expedition, Atmos. Chem. Phys., 23, 389-415,](#)

664 [doi:https://doi.org/10.5194/acp-23-389-2023,](https://doi.org/10.5194/acp-23-389-2023)

665 Burkart, J., Steiner, G., Reischl, G., and Hitznerberger, R.: Long-term study of cloud condensation  
666 nuclei (CCN) activation of the atmospheric aerosol in Vienna, Atmos Environ, 45, 5751-5759,  
667 [doi:https://doi.org/10.1016/j.atmosenv.2011.07.022](https://doi.org/10.1016/j.atmosenv.2011.07.022), 2011.

668 [Cai, M., Tan, H., Chan, C. K., Mochida, M., Hatakeyama, S., Kondo, Y., Schurman, M. I., Xu, H.,](#)  
669 [Li, F., Shimada, K., Li, L., Deng, Y., Yai, H., Matsuki, A., Qin, Y., and Zhao, J.:](#) Comparison of Aerosol  
670 Hygroscopicity, Volatility, and Chemical Composition between a Suburban Site in the Pearl River Delta  
671 Region and a Marine Site in Okinawa, Aerosol Air Qual Res, 17, 3194-3208,  
672 [doi:https://doi.org/10.4209/aaqr.2017.01.0020](https://doi.org/10.4209/aaqr.2017.01.0020), 2017.

673 Cai, M. F., Liang, B. L., Sun, Q. B., Zhou, S. Z., Chen, X. Y., Yuan, B., Shao, M., Tan, H. B., and  
674 Zhao, J.: Effects of continental emissions on cloud condensation nuclei (CCN) activity in the northern  
675 South China Sea during summertime 2018, Atmos. Chem. Phys., 20, 9153-9167,  
676 [doi:https://doi.org/10.5194/acp-20-9153-2020](https://doi.org/10.5194/acp-20-9153-2020), 2020.

677 Cai, M. F., Tan, H. B., Chan, C. K., Qin, Y. M., Xu, H. B., Li, F., Schurman, M. I., Liu, L., and Zhao,  
678 J.: The size-resolved cloud condensation nuclei (CCN) activity and its prediction based on aerosol  
679 hygroscopicity and composition in the Pearl Delta River (PRD) region during wintertime 2014, Atmos.  
680 Chem. Phys., 18, 16419-16437, [doi:https://doi.org/10.5194/acp-18-16419-2018](https://doi.org/10.5194/acp-18-16419-2018), 2018.

681 Chao, Q., Xiao, C., Li, w., Wang, L., Sun, L., Chen, X., Chen, Y., Li, Y., Gao, G., Liu, Y., Zhang,  
682 D., Ai, W., Chen, Y., Cui, T., Dai, T., Feng, A., Guo, Y., Huang, D., Jiang, Y., Li, D., Li, M., Liu, B., Liu,  
683 Y., Lv, Z., Mei, m., Wang, Q., Wang, Y., Yin, Y., Zeng, H., Zhang, Y., Zhai, J., Zhao, L., Zhi, R., Zhong,  
684 H., Zhou, X., Zhou, X., Zhu, X., and Wu, H.: China Climate Bulletin (2022), China Meteorological  
685 Administration, [https://www.cma.gov.cn/zfxxgk/gknr/qxbg/202303/t20230324\\_5396394.html](https://www.cma.gov.cn/zfxxgk/gknr/qxbg/202303/t20230324_5396394.html), 2022.

686 Choi, Y., Rhee, T. S., Collett, J. L., Park, T., Park, S.-M., Seo, B.-K., Park, G., Park, K., and Lee, T.:  
687 Aerosol concentrations and composition in the North Pacific marine boundary layer, Atmos Environ.,  
688 171, 165-172, [doi:https://doi.org/10.1016/j.atmosenv.2017.09.047](https://doi.org/10.1016/j.atmosenv.2017.09.047), 2017.

Formatted: Font: (Asian) +Body Asian (等线)

Deleted:

690 Crosbie, E., Youn, J. S., Balch, B., Wonaschutz, A., Shingler, T., Wang, Z., Conant, W. C., Betterton,  
691 E. A., and Sorooshian, A.: On the competition among aerosol number, size and composition in predicting  
692 CCN variability: a multi-annual field study in an urbanized desert, *Atmos Chem Phys*, 15, 6943-6958,  
693 doi:<https://doi.org/10.5194/acp-15-6943-2015>, 2015.

694 Deng, Z. Z., Zhao, C. S., Ma, N., Ran, L., Zhou, G. Q., Lu, D. R., and Zhou, X. J.: An examination  
695 of parameterizations for the CCN number concentration based on in situ measurements of aerosol  
696 activation properties in the North China Plain, *Atmos. Chem. Phys.*, 13, 6227-6237,  
697 doi:<https://doi.org/10.5194/acp-13-6227-2013>, 2013.

698 [Drinovec, L., Močnik, G., Zotter, P., Prévôt, A. S. H., Ruckstuhl, C., Coz, E., Rupakheti, M., Sciare,](#)  
699 [J., Müller, T., Wiedensohler, A., and Hansen, A. D. A.: The "dual-spot" Aethalometer: an](#)  
700 [improved measurement of aerosol black carbon with real-time loading compensation. \*Atmospheric\*](#)  
701 [Measurement Techniques](#), 8, 1965-1979, doi:<https://doi.org/10.5194/amt-8-1965-2015>, 2015.

702 Dusek, U., Frank, G. P., Hildebrandt, L., Curtius, J., Schneider, J., Walter, S., Chand, D., Drewnick,  
703 F., Hings, S., Jung, D., Borrmann, S., and Andreae, M. O.: Size matters more than chemistry for cloud-  
704 nucleating ability of aerosol particles, *Science*, 312, 1375-1378,  
705 doi:<https://doi.org/10.1126/science.1125261>, 2006.

706 [Ervens, B., Cubison, M. J., Andrews, E., Feingold, G., Ogren, J. A., Jimenez, J. L., Quinn, P. K.,](#)  
707 [Bates, T. S., Wang, J., Zhang, Q., Coe, H., Flynn, M., and Allan, J. D.: CCN predictions using simplified](#)  
708 [assumptions of organic aerosol composition and mixing state: a synthesis from six different locations,](#)  
709 [Atmos. Chem. Phys., 10, 4795-4807, doi:<https://doi.org/10.5194/acp-10-4795-2010>, 2010.](#)

710 Fitzgerald, J. W.: Dependence of the Supersaturation Spectrum of CCN on Aerosol Size Distribution  
711 and Composition, *J Atmos Sci*, 30, 628-634, doi:[https://doi.org/10.1175/1520-0469\(1973\)030](https://doi.org/10.1175/1520-0469(1973)030), 1973.

712 Fletcher, Squires, I. b. P., and Bowen, F. b. E. G.: *The Physics of Rainclouds*, 2011.

713 Geng, X. F., Zhong, G. C., Li, J., Cheng, Z. B., Mo, Y. Z., Mao, S. D., Su, T., Jiang, H. Y., Ni, K.  
714 W., and Zhang, G.: Molecular marker study of aerosols in the northern South China Sea: Impact of  
715 atmospheric outflow from the Indo-China Peninsula and South China, *Atmos Environ*, 206, 225-236,  
716 doi:<https://doi.org/10.1016/j.atmosenv.2019.02.033>, 2019.

Formatted: Font: (Asian) +Body Asian (等线)

Formatted: Font: (Asian) +Body Asian (等线)

717 Gras, J. L.: CN, CCN and particle size in Southern Ocean air at Cape Grim, Atmos Res, 35, 233-  
718 251, doi:[https://doi.org/10.1016/0169-8095\(94\)00021-5](https://doi.org/10.1016/0169-8095(94)00021-5), 1995.

719 Gras, J. L. and Keywood, M.: Cloud condensation nuclei over the Southern Ocean: wind  
720 dependence and seasonal cycles, Atmos. Chem. Phys., 17, 4419-4432, doi:[https://doi.org/10.5194/acp-](https://doi.org/10.5194/acp-17-4419-2017)  
721 17-4419-2017, 2017.

722 Gysel, M., Crosier, J., Topping, D. O., Whitehead, J. D., Bower, K. N., Cubison, M. J., Williams, P.  
723 I., Flynn, M. J., McFiggans, G. B., and Coe, H.: Closure study between chemical composition and  
724 hygroscopic growth of aerosol particles during TORCH2, Atmos. Chem. Phys., 7, 6131-6144,  
725 doi:<https://doi.org/10.5194/acp-7-6131-2007>, 2007.

726 [Heintzenberg, J.: Properties of the Log-Normal Particle Size Distribution, Aerosol Sci Tech, 21, 46-](#)  
727 [48, doi:<https://doi.org/10.1080/02786829408959695>, 1994.](#)

728 Huang, S., Wu, Z. J., Poulain, L., van Pinxteren, M., Merkel, M., Assmann, D., Herrmann, H., and  
729 Wiedensohler, A.: Source apportionment of the organic aerosol over the Atlantic Ocean from 53 degrees  
730 N to 53 degrees S: significant contributions from marine emissions and long-range transport, Atmos.  
731 Chem. Phys., 18, 18043-18062,doi: 10.5194/acp-18-18043-2018, 2018

732 Huang, S., Wu, Z., Wang, Y., Poulain, L., Höpner, F., Merkel, M., Herrmann, H., and Wiedensohler,  
733 A.: Aerosol Hygroscopicity and its Link to Chemical Composition in a Remote Marine Environment  
734 Based on Three Transatlantic Measurements, Environ. Sci. Technol, 56, 9613-9622,  
735 doi:<https://doi.org/10.1021/acs.est.2c00785>, 2022.

736 [Hussein, T., Dal Maso, M., Petäjä, T., Koponen, I., Paatero, P., Aalto, P., Hämeri, K., and Kulmala,](#)  
737 [M.: Evaluation of an automatic algorithm for fitting the particle number size distribution, Boreal Env.](#)  
738 [Res, 10, 337-355, 2005.](#)

739 IPCC: Annex I: Observational Products [Trewin, B. (ed.)], in: Climate Change 2021: The Physical  
740 Science Basis. Contribution of Working Group I to the Sixth Assessment Report of the Intergovernmental  
741 Panel on Climate Change, edited by: Masson-Delmotte, V., Zhai, P., Pirani, A., Connors, S. L., Péan, C.,  
742 Berger, S., Caud, N., Chen, Y., Goldfarb, L., Gomis, M. I., Huang, M., Leitzell, K., Lonnoy, E., Matthews,  
743 J. B. R., Maycock, T. K., Waterfield, T., Yelekçi, O., Yu, R., and Zhou, B., Cambridge University Press,

Formatted: Font: (Asian) +Body Asian (等线)

Formatted: Font: (Asian) +Body Asian (等线)



744 Cambridge, United Kingdom and New York, NY, USA, 2061–2086,  
745 <https://doi.org/10.1017/9781009157896.015>, 2021.

746 Jimenez, J. L., Canagaratna, M. R., Donahue, N. M., Prevot, A. S., Zhang, Q., Kroll, J. H., DeCarlo,  
747 P. F., Allan, J. D., Coe, H., Ng, N. L., Aiken, A. C., Docherty, K. S., Ulbrich, I. M., Grieshop, A. P.,  
748 Robinson, A. L., Duplissy, J., Smith, J. D., Wilson, K. R., Lanz, V. A., Hueglin, C., Sun, Y. L., Tian, J.,  
749 Laaksonen, A., Raatikainen, T., Rautiainen, J., Vaattovaara, P., Ehn, M., Kulmala, M., Tomlinson, J. M.,  
750 Collins, D. R., Cubison, M. J., Dunlea, E. J., Huffman, J. A., Onasch, T. B., Alfarra, M. R., Williams, P.  
751 I., Bower, K., Kondo, Y., Schneider, J., Drewnick, F., Borrmann, S., Weimer, S., Demerjian, K., Salcedo,  
752 D., Cottrell, L., Griffin, R., Takami, A., Miyoshi, T., Hatakeyama, S., Shimono, A., Sun, J. Y., Zhang, Y.  
753 M., Dzepina, K., Kimmel, J. R., Sueper, D., Jayne, J. T., Herndon, S. C., Trimborn, A. M., Williams, L.  
754 R., Wood, E. C., Middlebrook, A. M., Kolb, C. E., Baltensperger, U., and Worsnop, D. R.: Evolution of  
755 organic aerosols in the atmosphere, *Science*, 326, 1525-1529,  
756 doi:<https://doi.org/10.1126/science.1180353>, 2009.

757 Kawana, K., Miyazaki, Y., Omori, Y., Tanimoto, H., Kagami, S., Suzuki, K., Yamashita, Y., Nishioka,  
758 J., Deng, Y. G., Yai, H., and Mochida, M.: Number-Size Distribution and CCN Activity of Atmospheric  
759 Aerosols in the Western North Pacific During Spring Pre-Bloom Period: Influences of Terrestrial and  
760 Marine Sources, *J Geophys Res-Atmos*, 127, e2022JD036690,  
761 doi:<https://doi.org/10.1029/2022JD036690>, 2022.

762 Köhler, H.: The nucleus in and the growth of hygroscopic droplets, *Trans. Faraday Soc.*, 32, 1152-  
763 1161, doi:<https://doi.org/10.1039/TF9363201152>, 1936.

764 [Kouvarakis, G. and Mihalopoulos, N.: Seasonal variation of dimethylsulfide in the gas phase and](#)  
765 [of methanesulfonate and non-sea-salt sulfate in the aerosols phase in the Eastern Mediterranean](#)  
766 [atmosphere, \*Atmos Environ.\*, 36, 929-938, doi:\[https://doi.org/10.1016/s1352-2310\\(01\\)00511-8\]\(https://doi.org/10.1016/s1352-2310\(01\)00511-8\), 2002.](#)

767 Lambe, A. T., Onasch, T. B., Massoli, P., Croasdale, D. R., Wright, J. P., Ahern, A. T., Williams, L.  
768 R., Worsnop, D. R., Brune, W. H., and Davidovits, P.: Laboratory studies of the chemical composition  
769 and cloud condensation nuclei (CCN) activity of secondary organic aerosol (SOA) and oxidized primary  
770 organic aerosol (OPOA), *Atmos. Chem. Phys.*, 11, 8913-8928, doi:[https://doi.org/10.5194/acp-11-8913-](https://doi.org/10.5194/acp-11-8913-2011)  
771 2011, 2011.

Formatted: Font: (Asian) +Body Asian (等线)

772 Latham, T. L. and Nenes, A.: Water Vapor Depletion in the DMT Continuous-Flow CCN Chamber:  
773 Effects on Supersaturation and Droplet Growth, *Aerosol Sci Tech*, 45, 604-615,  
774 doi:<https://doi.org/10.1080/02786826.2010.551146>, 2011.

775 Leena, P. P., Pandithurai, G., Anilkumar, V., Murugavel, P., Sonbawne, S. M., and Dani, K. K.:  
776 Seasonal variability in aerosol, CCN and their relationship observed at a high altitude site in Western  
777 Ghats, *Meteorol Atmos Phys*, 128, 143-153, doi:<https://doi.org/10.1007/s00703-015-0406-0>, 2016.

778 Liang, B., Cai, M., Sun, Q., Zhou, S., and Zhao, J.: Source apportionment of marine atmospheric  
779 aerosols in northern South China Sea during summertime 2018, *Environ. Pollut*, 289, 117948,  
780 doi:<https://doi.org/10.1016/j.envpol.2021.117948>, 2021.

781 Liu, P., Song, M., Zhao, T., Gunthe, S. S., Ham, S., He, Y., Qin, Y. M., Gong, Z., Amorim, J. C.,  
782 Bertram, A. K., and Martin, S. T.: Resolving the mechanisms of hygroscopic growth and cloud  
783 condensation nuclei activity for organic particulate matter, *Nat. Commun*, 9, 4076,  
784 doi:<https://doi.org/10.1038/s41467-018-06622-2>, 2018.

785 Liu, X. and Wang, J.: How important is organic aerosol hygroscopicity to aerosol indirect forcing?,  
786 *Environ. Res. Lett*, 5, 044010, doi:<https://doi.org/10.1088/1748-9326/5/4/044010>, 2010.

787 Liu, Y., Sun, L., Zhou, X., Luo, Y., Huang, W., Yang, C., Wang, Y., and Huang, T.: A 1400-year  
788 terrigenous dust record on a coral island in South China Sea, *Sci Rep*, 4, 4994,  
789 doi:<https://doi.org/10.1038/srep04994>, 2014.

790 [Meng, J. W., Yeung, M. C., Li, Y. J., Lee, B. Y. L., and Chan, C. K.:](#) Size-resolved cloud  
791 condensation nuclei (CCN) activity and closure analysis at the HKUST Supersite in Hong Kong, *Atmos.*  
792 *Chem. Phys.*, 14, 10267-10282, doi:<https://doi.org/10.5194/acp-14-10267-2014>, 2014.

793 [Miller, R. M., Rauber, R. M., Di Girolamo, L., Rilloraza, M., Fu, D., McFarquhar, G. M., Nesbitt,](#)  
794 [S. W., Ziemba, L. D., Woods, S., and Thornhill, K. L.:](#) Influence of natural and anthropogenic aerosols  
795 [on cloud base droplet size distributions in clouds over the South China Sea and West Pacific.](#) *Atmos.*  
796 *Chem. Phys.*, 23, 8959-8977, doi:<https://doi.org/10.5194/acp-23-8959-2023>, 2023.

**Deleted:** Lu, W., Yang, S., Zhu, W., Li, X., Cui, S., Luo, T., Han, L., and Shi, J.: Evaluation of High Cloud Product of ECMWF Over South China Sea Using CALIOP, *Earth Space Sci*, 9, e2021EA002113, doi:<https://doi.org/10.1029/2021ea002113>, 2022.

802 Moore, R. H., Nenes, A., and Medina, J.: Scanning Mobility CCN Analysis-A Method for Fast  
803 Measurements of Size-Resolved CCN Distributions and Activation Kinetics, *Aerosol Sci Tech*, 44, 861-  
804 871, doi:<https://doi.org/10.1080/02786826.2010.498715>, 2010.

805 Ou, H., Cai, M., Zhang, Y., Ni, X., Liang, B., Sun, Q., Mai, S., Sun, C., Zhou, S., Wang, H., Sun, j.,  
806 and Zhao, J.: Measurement Report: Seasonal variation and anthropogenic influence on cloud  
807 condensation nuclei (CCN) activity in the South China Sea: Insights from shipborne observations during  
808 summer and winter of 2021 [dataset], doi:<https://doi.org/10.6084/m9.figshare.25472545>, 2024.

809 Ovadnevaite, J., Zuend, A., Laaksonen, A., Sanchez, K. J., Roberts, G., Ceburnis, D., Decesari, S.,  
810 Rinaldi, M., Hodas, N., Facchini, M. C., Seinfeld, J. H., and O' Dowd, C.: Surface tension prevails over  
811 solute effect in organic-influenced cloud droplet activation, *Nature*, 546, 637-641,  
812 doi:<https://doi.org/10.1038/nature22806>, 2017.

813 [Padró, L. T., Moore, R. H., Zhang, X., Rastogi, N., Weber, R. J., and Nenes, A.: Mixing state and](#)  
814 [compositional effects on CCN activity and droplet growth kinetics of size-resolved CCN in an urban](#)  
815 [environment, \*Atmos. Chem. Phys.\*, 12, 10239-10255, doi:<https://doi.org/10.5194/acp-12-10239-2012>.](#)  
816 [2012.](#)

817 Park, M., Yum, S. S., Kim, N., Cha, J. W., Shin, B., and Ryoo, S.-B.: Characterization of submicron  
818 aerosols and CCN over the Yellow Sea measured onboard the Gisang 1 research vessel using the positive  
819 matrix factorization analysis method, *Atmos Res*, 214, 430-441,  
820 doi:<https://doi.org/10.1016/j.atmosres.2018.08.015>, 2018.

821 Patel, P. N. and Jiang, J. H.: Cloud condensation nuclei characteristics at the Southern Great Plains  
822 site: role of particle size distribution and aerosol hygroscopicity, *Environ Res Commun*, 3,  
823 doi:<https://doi.org/10.1088/2515-7620/ac0e0b>, 2021

824 Petters, M. D. and Kreidenweis, S. M.: A single parameter representation of hygroscopic growth  
825 and cloud condensation nucleus activity, *Atmos. Chem. Phys.*, 7, 1961-1971,  
826 doi:<https://doi.org/10.5194/acp-7-1961-2007>, 2007.

827 Pöhlker, M. L., Pöhlker, C., Ditas, F., Klimach, T., Hrabe de Angelis, I., Araújo, A., Brito, J.,  
828 Carbone, S., Cheng, Y., Chi, X., Ditz, R., Gunthe, S. S., Kesselmeier, J., Könemann, T., Lavrič, J. V.,

829 Martin, S. T., Mikhailov, E., Moran-Zuloaga, D., Rose, D., Saturno, J., Su, H., Thalman, R., Walter, D.,  
830 Wang, J., Wolff, S., Barbosa, H. M. J., Artaxo, P., Andreae, M. O., and Pöschl, U.: Long-term  
831 observations of cloud condensation nuclei in the Amazon rain forest – Part 1: Aerosol size distribution,  
832 hygroscopicity, and new model parametrizations for CCN prediction, *Atmos. Chem. Phys.*, 16, 15709-  
833 15740, doi:<https://doi.org/10.5194/acp-16-15709-2016>, 2016.

834 Qin, Y., Wang, H., Wang, Y., Lu, X., Tang, H., Zhang, J., Li, L., and Fan, S.: Wildfires in Southeast  
835 Asia pollute the atmosphere in the northern South China Sea, *Sci Bull (Beijing)*, 69, 1011-1015,  
836 doi:<https://doi.org/10.1016/j.scib.2024.02.026>, 2024.

837 Quinn, P. K., Bates, T. S., Coffman, D. J., and Covert, D. S.: Influence of particle size and chemistry  
838 on the cloud nucleating properties of aerosols, *Atmos. Chem. Phys.*, 8, 1029-1042,  
839 doi:<https://doi.org/10.5194/acp-8-1029-2008>, 2008.

840 Quinn, P. K., Bates, T. S., Coffman, D. J., Upchurch, L., Johnson, J. E., Moore, R., Ziemba, L., Bell,  
841 T. G., Saltzman, E. S., Graff, J., and Behrenfeld, M. J.: Seasonal Variations in Western North Atlantic  
842 Remote Marine Aerosol Properties, *J Geophys Res-Atmos*, 124, 14240-14261,  
843 doi:<https://doi.org/10.1029/2019jd031740>, 2019.

844 Rose, D., Nowak, A., Achtert, P., Wiedensohler, A., Hu, M., Shao, M., Zhang, Y., Andreae, M. O.,  
845 and Pöschl, U.: Cloud condensation nuclei in polluted air and biomass burning smoke near the mega-city  
846 Guangzhou, China - Part 1: Size-resolved measurements and implications for the modeling of aerosol  
847 particle hygroscopicity and CCN activity, *Atmos. Chem. Phys.*, 10, 3365-3383,  
848 doi:<https://doi.org/10.5194/acp-10-3365-2010>, 2010.

849 Ross, K. E., Piketh, S. J., Bruintjes, R. T., Burger, R. P., Swap, R. J., and Annegarn, H. J.: Spatial  
850 and seasonal variations in CCN distribution and the aerosol-CCN relationship over southern Africa, *J*  
851 *Geophys Res-Atmos*, 108, doi:<https://doi.org/10.1029/2002jd002384>, 2003.

852 Safai, P. D., Raju, M. P., Rao, P. S. P., and Pandithurai, G.: Characterization of carbonaceous aerosols  
853 over the urban tropical location and a new approach to evaluate their climatic importance, *Atmos Environ*,  
854 92, 493-500, doi:<https://doi.org/10.1016/j.atmosenv.2014.04.055>, 2014.

855 Sarangi, B., Ramachandran, S., Rajesh, T. A., and Dhaker, V. K.: Black carbon linked aerosol  
856 hygroscopic growth: Size and mixing state are crucial, *Atmos Environ.*, 200, 110-118,  
857 doi:<https://doi.org/https://doi.org/10.1016/j.atmosenv.2018.12.001>, 2019.

858 Schmale, J., Henning, S., Decesari, S., Henzing, B., Keskinen, H., Sellegri, K., Ovadnevaite, J.,  
859 Pohlker, M. L., Brito, J., Bougiatioti, A., Kristensson, A., Kalivitis, N., Stavroulas, I., Carbone, S.,  
860 Jefferson, A., Park, M., Schlag, P., Iwamoto, Y., Aalto, P., Aijala, M., Bukowiecki, N., Ehn, M., Frank,  
861 G., Frohlich, R., Frumau, A., Herrmann, E., Herrmann, H., Holzinger, R., Kos, G., Kulmala, M.,  
862 Mihalopoulos, N., Nenes, A., O'Dowd, C., Petaja, T., Picard, D., Pohlker, C., Poschl, U., Poulain, L.,  
863 Prevot, A. S. H., Swietlicki, E., Andreae, M. O., Artaxo, P., Wiedensohler, A., Ogren, J., Matsuki, A.,  
864 Yum, S. S., Stratmann, F., Baltensperger, U., and Gysel, M.: Long-term cloud condensation nuclei  
865 number concentration, particle number size distribution and chemical composition measurements at  
866 regionally representative observatories, *Atmos. Chem. Phys.*, 18, 2853-2881,  
867 doi:<https://doi.org/10.5194/acp-18-2853-2018>, 2018.

868 Seinfeld, J. H. and Pandis, S. N.: *Atmospheric Chemistry and Physics: From Air Pollution to*  
869 *Climate Change*, Wiley 2016.

870 Sihto, S. L., Mikkila, J., Vanhanen, J., Ehn, M., Liao, L., Lehtipalo, K., Aalto, P. P., Duplissy, J.,  
871 Petaja, T., Kerminen, V. M., Boy, M., and Kulmala, M.: Seasonal variation of CCN concentrations and  
872 aerosol activation properties in boreal forest, *Atmos. Chem. Phys.*, 11, 13269-13285,  
873 doi:<https://doi.org/10.5194/acp-11-13269-2011>, 2011.

874 [Su, H., Rose, D., Cheng, Y. F., Gunthe, S. S., Massling, A., Stock, M., Wiedensohler, A., Andreae,](#)  
875 [M. O., and Pöschl, U.: Hygroscopicity distribution concept for measurement data analysis and modeling](#)  
876 [of aerosol particle mixing state with regard to hygroscopic growth and CCN activation, \*Atmos. Chem.\*](#)  
877 [Phys., 10, 7489-7503, doi:<https://doi.org/10.5194/acp-10-7489-2010>, 2010.](#)

878 [Sun, C., Zhang, Y., Liang, B., Gao, M., Sun, X., Li, F., Ni, X., Sun, Q., Ou, H., Chen, D., Zhou, S.,](#)  
879 [and Zhao, J.: Morphological and optical properties of carbonaceous aerosol particles from ship emissions](#)  
880 [and biomass burning during a summer cruise measurement in the South China Sea, \*Atmos. Chem. Phys.\*,](#)  
881 [24, 3043-3063, doi:<https://doi.org/10.5194/acp-24-3043-2024>, 2024.](#)

Formatted: Font: (Asian) +Body Asian (等线)

882 Sun, Q., Liang, B., Cai, M., Zhang, Y., Ou, H., Ni, X., Sun, X., Han, B., Deng, X., Zhou, S., and  
883 Zhao, J.: Cruise observation of the marine atmosphere and ship emissions in South China Sea: Aerosol  
884 composition, sources, and the aging process, Environ. Pollut, 316, 120539,  
885 doi:https://doi.org/10.1016/j.envpol.2022.120539, 2023.

886 Wang, B., Huang, F., Wu, Z., Yang, J., Fu, X., and Kikuchi, K.: Multi-scale climate variability of  
887 the South China Sea monsoon: A review, Dynam Atmos Oceans, 47, 15-37,  
888 doi:https://doi.org/10.1016/j.dynatmoce.2008.09.004, 2009. Wang, Y., Chen, J., Wang, Q., Qin, Q., Ye, J.,  
889 Han, Y., Li, L., Zhen, W., Zhi, Q., Zhang, Y., and Cao, J.: Increased secondary aerosol contribution and  
890 possible processing on polluted winter days in China, Environ Int, 127, 78-84,  
891 doi:https://doi.org/10.1016/j.envint.2019.03.021, 2019.

892 [Wang, J., Cubison, M. J., Aiken, A. C., Jimenez, J. L., and Collins, D. R.: The importance of aerosol](#)  
893 [mixing state and size-resolved composition on CCN concentration and the variation of the importance](#)  
894 [with atmospheric aging of aerosols, Atmos. Chem. Phys., 10, 7267-7283,](#)  
895 [doi:https://doi.org/10.5194/acp-10-7267-2010, 2010.](#)

896 [Wang, Q., and Sun, Y.: Characterization of aerosol hygroscopicity, mixing state, and CCN activity](#)  
897 [at a suburban site in the central North China Plain, Atmos. Chem. Phys., 18, 11739-11752,](#)  
898 [doi:https://doi.org/10.5194/acp-18-11739-2018, 2018,](#)

899 Wang, Y. Q.: MeteoInfo: GIS software for meteorological data visualization and analysis, Meteorol.  
900 Appl, 21, 360-368, doi:https://doi.org/10.1002/met.1345, 2014.

901 [Xiao, H.-W., Xiao, H.-Y., Luo, L., Shen, C.-Y., Long, A.-M., Chen, L., Long, Z.-H., and Li, D.-N.:](#)  
902 [Atmospheric aerosol compositions over the South China Sea: temporal variability and source](#)  
903 [apportionment, Atmos. Chem. Phys., 17, 3199-3214, doi:https://doi.org/10.5194/acp-17-3199-2017,](#)  
904 [2017.](#)

905 [Zheng, G., Kuang, C., Uin, J., Watson, T., and Wang, J.: Large contribution of organics to](#)  
906 [condensational growth and formation of cloud condensation nuclei \(CCN\) in the remote marine boundary](#)  
907 [layer, Atmos. Chem. Phys., 20, 12515-12525, doi:https://doi.org/10.5194/acp-20-12515-2020, 2020.](#)

Formatted: Font: (Asian) +Body Asian (等线)

Deleted:

Deleted:

Formatted: 参考文献, Space After: 7.8 pt

910 [Zhu, K. and Wang, L.: A comprehensive study on the validation and application of multi-lognormal](#)  
911 [distribution models for atmospheric particles, Atmos Environ., 338, 120813,](#)  
912 [doi:https://doi.org/10.1016/j.atmosenv.2024.120813, 2024.](#)

913

Formatted: Indent: First line: 2 ch

Location	period	$N_{CN}$ ( $\text{cm}^{-3}$ )	$N_{CCN}$ ( $\text{cm}^{-3}$ )	Hygroscopicity ( $\kappa$ )	Bulk AR	$D_{50}$ (nm)	Reference
South China Sea	2021.05.05-	6966±9249	2640±3639 (0.20% SS)	0.47±0.21 (0.20% SS)	0.37±0.16 (0.20% SS)	96±19 (0.20% SS)	This study
	2021.06.09		4392±6415 (0.40% SS)	0.54±0.21 (0.40% SS)	0.63±0.17 (0.40% SS)	57±9 (0.40% SS)	
			5215±6862 (0.70% SS)	0.87±0.17 (0.70% SS)	0.87±0.17 (0.70% SS)		
Northern South China Sea	2021.12.19-	4988±3474	1086±691 (0.10% SS)	0.50±0.21 (0.10% SS)	0.23±0.09 (0.10% SS)	145±18 (0.10% SS)	This study
	2021.12.29		1625±1110 (0.20% SS)	0.31±0.10 (0.20% SS)	0.33±0.12 (0.20% SS)	107±13 (0.20% SS)	
			2218±1503 (0.40% SS)	0.19±0.05 (0.40% SS)	0.44±0.13 (0.40% SS)	79±7 (0.40% SS)	
Northern South China Sea	2018.08.06-	3463	1544 (0.34% SS)	0.38±0.09 (0.18% SS)	/	/	Cai et al., 2020
	2018.08.27		0.40±0.08 (0.34% SS)				
			0.38±0.08 (0.59% SS)				
Remote South China Sea	2012.09.14-	503±455	450±388 (0.14% SS)	0.54±0.14 (0.14% SS)	0.47±0.16 (0.14% SS)	/	Atwood et al., 2017
	2012.09.26		675±516 (0.38% SS)	0.54±0.14 (0.14% SS)	0.72±0.17 (0.38% SS)		
			698±555 (0.53% SS)	0.50±0.21 (0.38% SS)	0.79±0.15 (0.53% SS)		
Western North Pacific	2015.03.04-	/	/	0.75±0.21 (0.11% SS)	0.40±0.22 (0.11% SS)	/	Kawana et al., 2020
	2015.03.26		0.51±0.16 (0.24% SS)	0.50±0.22 (0.24% SS)			
			0.45±0.16 (0.60% SS)	0.70±0.23 (0.60% SS)			
Guangzhou	2014.11-	/	3103±1913 (0.10% SS)	0.37±0.11 (0.10% SS)	0.26±0.10 (0.10% SS)	156 ± 19 (0.1% SS)	Cai et al., 2018
	2014.12		5095±2972 (0.20% SS)	0.29±0.09 (0.20% SS)	0.41±0.14 (0.20% SS)	107 ± 17 (0.2% SS)	
			6524±3783 (0.40% SS)	0.18±0.07 (0.40% SS)	0.53±0.15 (0.40% SS)	78 ± 15 (0.4% SS)	
			7913±4234 (0.70% SS)	0.15±0.06 (0.70% SS)	0.64±0.13 (0.70% SS)	58 ± 11 (0.7% SS)	

**Deleted:** Table 1. The number concentration of particle and cloud condensation nuclei at different supersaturation (SS), the hygroscopicity and bulk activation ratio (AR), and activation diameter ( $D_{50}$ ) at different SS in different studies.



Yellow Sea	2017.04- 2017.05	7622± 4038	4821±1763 (0.63% SS)	/	/	/	Park et al., 2018
------------	---------------------	---------------	----------------------	---	---	---	-------------------

919 [Table 1. The number concentration of particle and cloud condensation nuclei at different supersaturation \(SS\), the hygroscopicity and bulk activation ratio \(AR\), and activation](#)  
920 [diameter \(D<sub>50</sub>\) at different SS in different studies.](#)

**Formatted:** Normal, Indent: First line: 0 cm,  
Space After: 0 pt

921

Cluster	Summer			Winter		
	Indochinese Peninsula	Luzon	Marine	Mainland China	Marine	Mixed
$N_{CCN}$ ( $cm^{-3}$ )						
0.1% SS	\	\	\	1359±669	439±223	945±400
0.2% SS	1200±787	4066±4748	1135±800	2058±1095	614±318	1460±514
0.4% SS	1650±1187	7804±8608	1812±1052	2792±1478	830±424	1801±640
0.7% SS	2239±1367	10480±9741	2515±1523	3514±1841	1024±463	2101±757
$N_{CN}$ ( $cm^{-3}$ )						
Total	2699±2147	14674±13844	3033±2366	6875±3263	1728±465	2918±1204
Nucleation	111±206	1543±3341	238±426	893±925	214±281	141±191
Aikten	1156±1261	8653±8815	1668±1526	3089±2017	732±337	806±427
Accumulation	1434±1444	3764±4157	1121±929	2923±2440	781±313	1975±831
Bulk AR						
0.1% SS	\	\	\	0.21±0.07	0.26±0.10	0.32±0.04
0.2% SS	0.49±0.13	0.31±0.17	0.40±0.13	0.30±0.09	0.36±0.14	0.51±0.05
0.4% SS	0.73±0.09	0.55±0.18	0.68±0.14	0.40±0.10	0.49±0.16	0.63±0.06
0.7% SS	0.98±0.15	0.76±0.16	0.90±0.13	0.50±0.09	0.61±0.18	0.73±0.06

Moved down [9]: Table 2. The number concentration of particle, cloud condensation nuclei, and bulk activation ratio in different periods.

922 Table 2. The number concentration of particle, cloud condensation nuclei, and bulk activation ratio in  
 923 different periods.

Formatted: Indent: First line: 0 ch

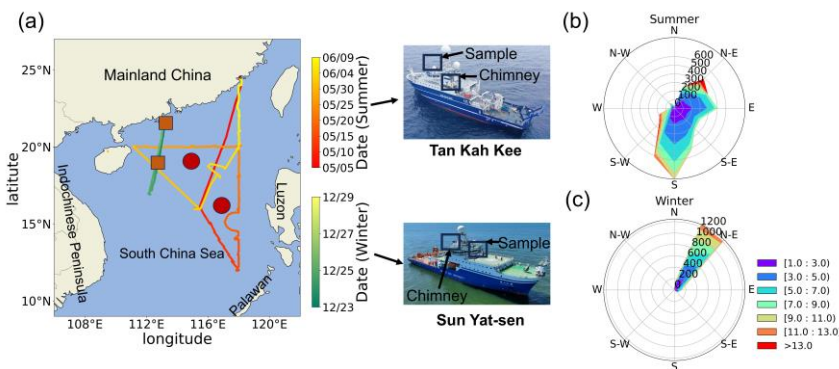
924

Cluster	Summer			Winter		
	Luzon	Indochinese Peninsula	Marine	Mainland China	Mixed	Marine
<b>Internal scheme</b>						
0.1% SS	\	\	\	0.91 (0.97)	0.72 (0.95)	0.71 (0.94)
0.2% SS	0.83 (0.89)	0.89 (0.81)	0.76 (0.96)	1.13 (0.96)	1.01 (0.99)	0.94 (0.97)
0.4% SS	0.90 (0.96)	0.90 (0.98)	0.89 (0.97)	1.34 (0.97)	1.14 (0.98)	1.04 (0.98)
0.7% SS	0.91 (0.93)	0.96 (0.92)	0.88 (0.98)	1.38 (0.97)	1.16 (0.99)	1.04 (0.96)
<b>External scheme</b>						
0.1% SS	\	\	\	0.80 (0.97)	0.62 (0.95)	0.59 (0.94)
0.2% SS	0.74 (0.88)	0.77 (0.79)	0.80 (0.96)	1.01 (0.97)	0.90 (0.99)	0.81 (0.97)
0.4% SS	0.78 (0.93)	0.80 (0.97)	0.82 (0.96)	1.23 (0.97)	1.05 (0.98)	0.95 (0.98)
0.7% SS	0.80 (0.92)	0.89 (0.92)	0.80 (0.98)	1.24 (0.98)	1.11 (0.99)	1.00 (0.96)

Moved down [8]: Table 3. The slope and coefficient of determination (in parentheses) in CCN closure analysis at different supersaturations in different periods.

Table 3. The slope and coefficient of determination (in parentheses) in CCN closure analysis at different supersaturations in different periods.

Moved (insertion) [8]



936

937 **Figure 1.** The cruises of two shipborne observations, and the location of sample line and chimney of  
 938 Tan Kah Kee, and Sun Yat-sen scientific vessel (a); Wind rose of the wind direction and wind speed in  
 939 summer and winter cruises; The radius represents the frequency of wind direction occurrences, and the  
 940 shaded areas indicate wind speed (b) and (c). The red circles are the midpoints of the ship trajectory  
 941 selected for backward trajectory and cluster analysis in summer and the orange squares are the  
 942 midpoints of the ship trajectory selected for backward trajectory and cluster analysis in winter.

**Moved down [1]:** Figure 1. The cruises of two shipborne observations, and the location of sample line and chimney of Tan Kah Kee, and Sun Yat-sen scientific vessel (a); Wind rose of the wind direction and wind speed in summer and winter cruises; The radius represents the frequency of wind direction occurrences, and the shaded areas indicate wind speed (b) and (c). The red circles are the midpoints of the ship trajectory selected for backward trajectory and cluster analysis in summer and the orange squares are the midpoints of the ship trajectory selected for backward trajectory and cluster analysis in winter.

**Moved down [2]:** Figure 2. Timeseries of (a) particle number size distribution, (b) mass concentration of NR-PM<sub>1</sub>, and (c) its fraction, (d) mass concentration of organic carbon and elemental carbon, (e) number concentration of total particle and cloud condensation nuclei under the supersaturation of 0.1%, 0.2%, 0.4%, and 0.7%, and (f) aerosol hygroscopicity. The number 1 in figure number means timeseries in summer and number 2 means it in winter.

**Moved down [3]:** Figure 3. Particle number size distribution in summer (a) and winter (b); The red markers represent the activation diameters and hygroscopicity parameters corresponding to 0.1%, 0.2%, 0.4%, and 0.7% supersaturations in this study (without 0.1% in summer). The green markers represent the hygroscopicity parameters reported in Atwood et al. (2017) for the southern South China Sea during summer. The gray markers represent the hygroscopicity parameters documented in Cai et al. (2018) for the Pearl River Delta region during winter. The fraction of NR-PM<sub>1</sub> in summer (c) and winter (d) in this study, in northern SCS reported by Liang et al. (2021) (e), and in North Pacific reported by Choi et al. (2017) (f).

**Moved down [4]:** Figure 4. The cluster analysis result in summer (a) and winter (b). The solid line in summer means cluster analysis from May 5 to May 24 and the dash line in summer means cluster analysis from May 25 to June 9; The

**Moved down [5]:** Figure 5. The fraction of NR-PM<sub>1</sub> in “Luzon” period (a), “Indochinese Peninsula” period (b), and “Marine-s” period (c) in summer. The fraction of NR-PM<sub>1</sub> in

**Moved down [6]:** Figure 6. The particle number size distribution (PNSD) in “Luzon” period (a), “Indochinese Peninsula” period (b), and “Marine-s” period (c) in summer.

**Moved down [7]:** Figure 8. The normalized mean bias (NMB) calculated by “Internal-mixed” scheme and “External-mixed” scheme according to CCN closure method. The marker of circle means “Internal-mixed” scheme and the

**Deleted:** FIGURE CAPTION

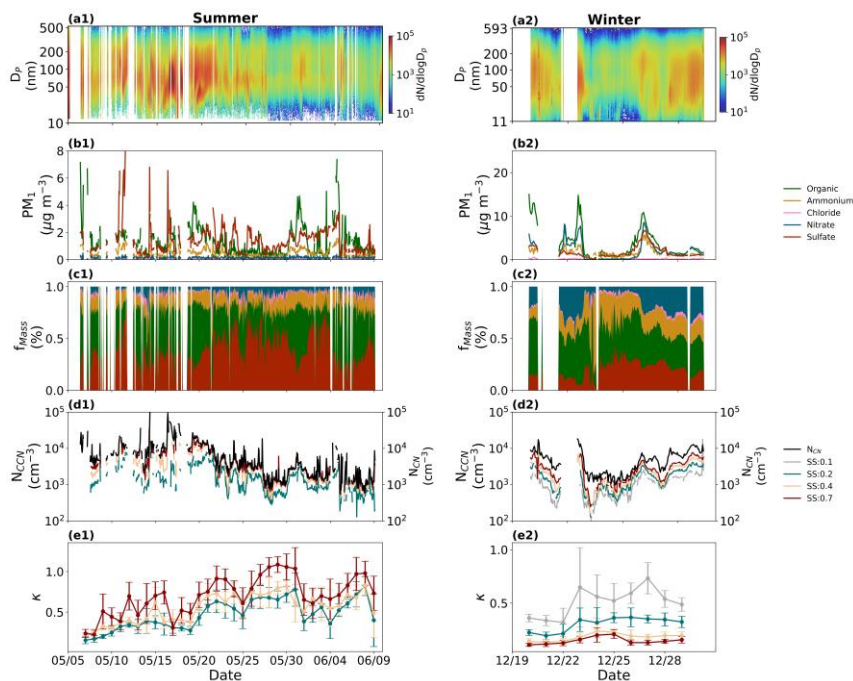
**Deleted:** Figure 7. The bulk activation ratio (AR) at different supersaturation (SS) in different periods (a); The aerosol hygroscopicity ( $\kappa$ ) at different supersaturation (SS) in different periods (b).

**Deleted:**  
 .....Page Break.....

**Moved (insertion) [1]**

**Deleted:**  
 Fig. 1

1022

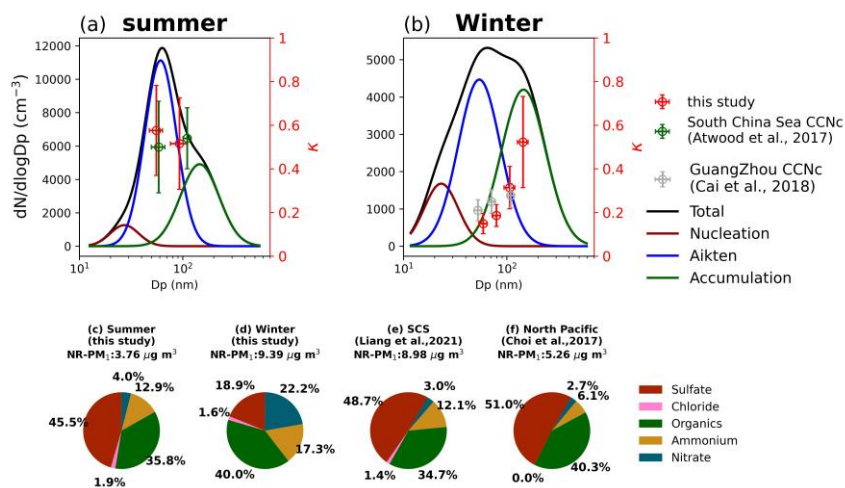


1023

1024 Figure 2. Timeseries of (a) particle number size distribution, (b) mass concentration of NR-PM1, and  
 1025 (c) its fraction, (d) mass concentration of organic carbon and elemental carbon, (e) number  
 1026 concentration of total particle and cloud condensation nuclei under the supersaturation of 0.1%, 0.2%,  
 1027 0.4%, and 0.7%, and (f) aerosol hygroscopicity. The number 1 in figure number means timeseries in  
 1028 summer and number 2 means it in winter.

Moved (insertion) [2]

Deleted: Fig. 2

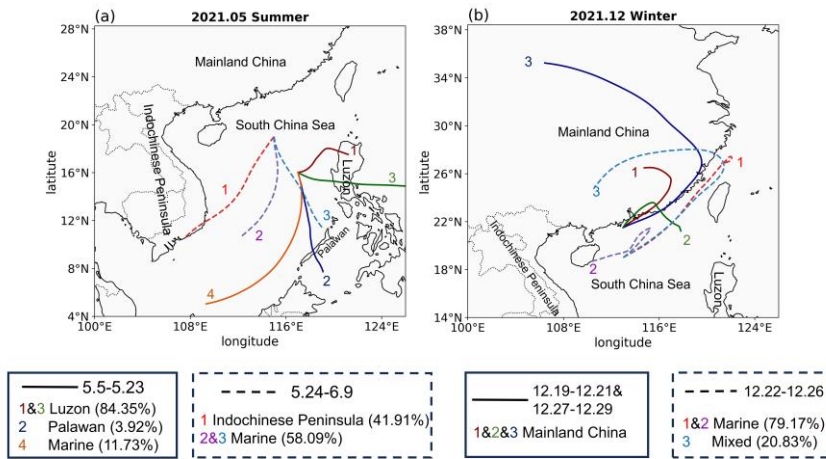


1031  
 1032 Figure 3. Particle number size distribution in summer (a) and winter (b); The red markers represent the  
 1033 activation diameters and hygroscopicity parameters corresponding to 0.1%, 0.2%, 0.4%, and 0.7%  
 1034 supersaturations in this study (without 0.1% in summer). The green markers represent the  
 1035 hygroscopicity parameters reported in Atwood et al. (2017) for the southern South China Sea during  
 1036 summer. The gray markers represent the hygroscopicity parameters documented in Cai et al. (2018)  
 1037 for the Pearl River Delta region during winter. The fraction of NR-PM<sub>2.5</sub> in summer (c) and winter (d) in  
 1038 this study, in northern SCS reported by Liang et al. (2021) (e), and in North Pacific reported by Choi et  
 1039 al. (2017) (f).

Moved (insertion) [3]

Formatted: Subscript

Deleted: Fig. 3



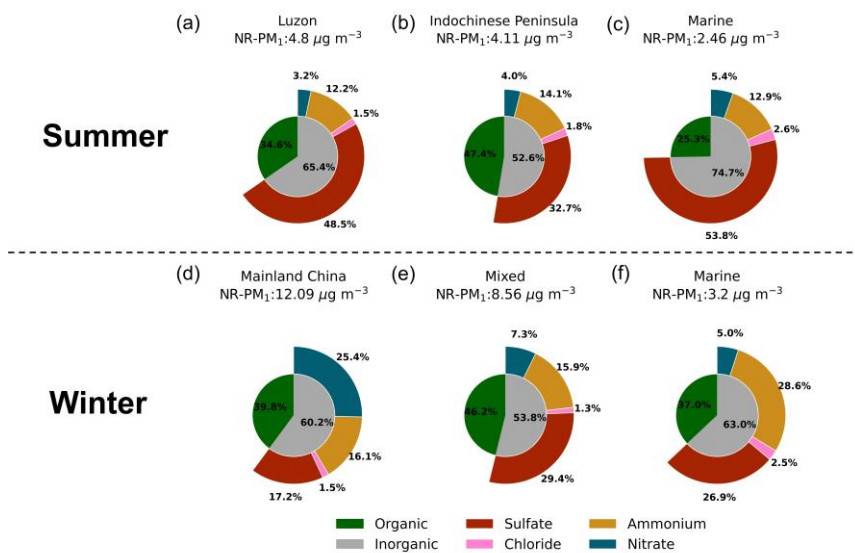
1041

1042 Figure 4. The cluster analysis results in summer (a) and winter (b). The solid line in summer means  
 1043 cluster analysis from May 5 to May 24 and the dash line in summer means cluster analysis from May  
 1044 25 to June 9; The solid line in winter means cluster analysis from Dec 19 to Dec 21 and Dec 27 to Dec  
 1045 29, and the dash line in winter means cluster analysis from Dec 22 to Dec 26.

Moved (insertion) [4]

Deleted: result

Deleted: Fig. 4



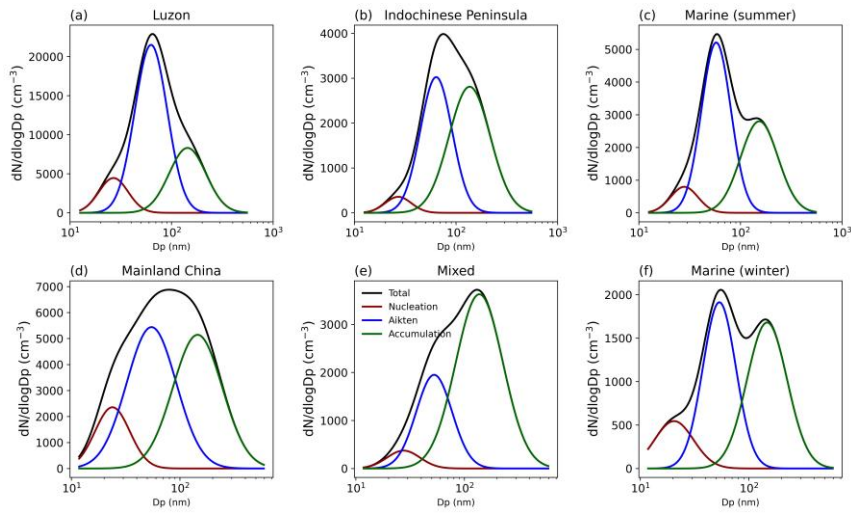
050 Figure 5. The fraction of NR-PM<sub>1</sub> in “Luzon” period (a), “Indochinese Peninsula” period (b), and  
 051 “Marine-s” period (c) in summer. The fraction of NR-PM<sub>1</sub> in “Mainland China” period (d), “Mixed”  
 052 period (e), and “Marine-w” period (f) in winter.

Moved (insertion) [5]

Deleted: Fig.5



1054



1055

1056

1057

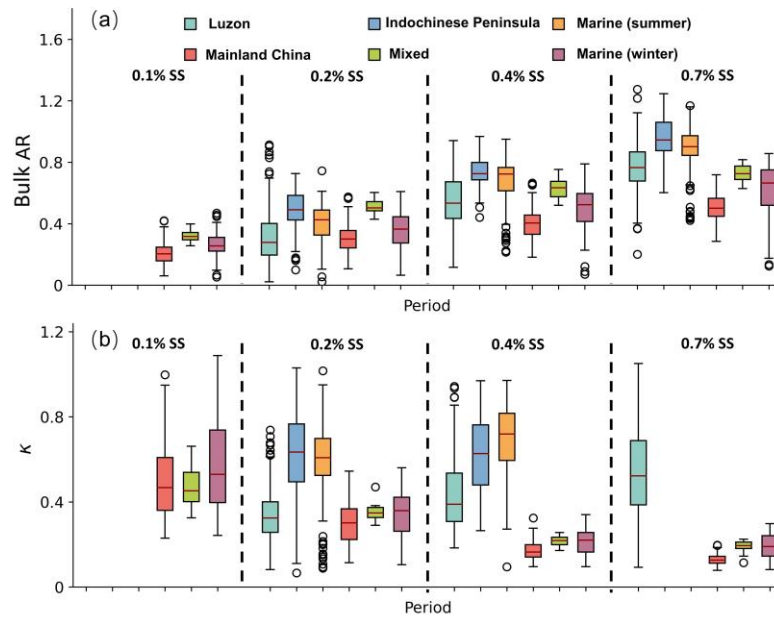
1058

Figure 6. The particle number size distribution (PNSD) in “Luzon” period (a), “Indochinese Peninsula” period (b), and “Marine-s” period (c) in summer. The PNSD in “Mainland China” period (d), “Mixed” period (e), and “Marine-w” period (f) in winter.

Moved (insertion) [6]

Deleted: Fig. 6

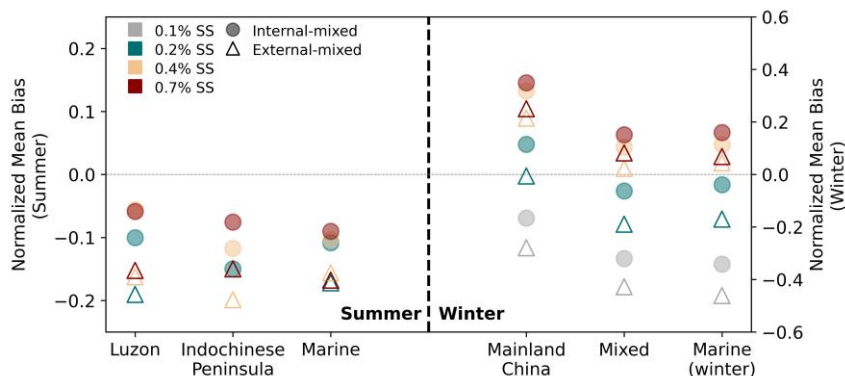
1060



1061

1062 [Figure 7. The bulk activation ratio \(AR\) at different supersaturation \(SS\) in different periods \(a\); The](#)  
1063 [aerosol hygroscopicity \( \$\kappa\$ \) at different supersaturation \(SS\) in different periods \(b\).](#)

Deleted: Fig. 7



Moved (insertion) [7]

Deleted: Fig. 8

Deleted: Beddows, D. C. S., Harrison, R. M., Green, D. C., and Fuller, G. W.: Receptor modelling of both particle composition and size distribution from a background site in London, UK, *Atmos. Chem. Phys.*, 15, 10107-10125, doi:<https://doi.org/10.5194/acp-15-10107-2015>, 2015.

Chao, Q., Xiao, C., Li, W., Wang, L., Sun, L., Chen, X., Chen, Y., Li, Y., Gao, G., Liu, Y., Zhang, D., Ai, W., Chen, Y., Cui, T., Dai, T., Feng, A., Guo, Y., Huang, D., Jiang, Y., Li, D., Li, M., Liu, B., Liu, Y., Lv, Z., Mei, M., Wang, Q., Wang, Y., Yin, Y., Zeng, H., Zhang, Y., Zhai, J., Zhao, L., Zhi, R., Zhong, H., Zhou, X., Zhou, X., Zhu, X., and Wu, H.: China Climate Bulletin (2022), China Meteorological Administration, [https://www.cma.gov.cn/zfxk/gk/gknr/qxbg/202303/t20230324\\_5396394.html](https://www.cma.gov.cn/zfxk/gk/gknr/qxbg/202303/t20230324_5396394.html), 2022.

Drinovec, L., Močnik, G., Zotter, P., Prévôt, A. S. H., Ruckstuhl, C., Coz, E., Rupakheti, M., Sciare, J., Müller, T., Wiedensohler, A., and Hansen, A. D. A.: The “dual-spot” Aethalometer: an improved measurement of aerosol black carbon with real-time loading compensation, *Atmospheric Measurement Techniques*, 8, 1965-1979, doi:<https://doi.org/10.5194/amt-8-1965-2015>, 2015.

Huang, S., Wu, Z., Wang, Y., Poulain, L., Höpner, F., Merkel, M., Herrmann, H., and Wiedensohler, A.: Aerosol Hygroscopicity and its Link to Chemical Composition in a Remote Marine Environment Based on Three Transatlantic Measurements, *Environmental Science & Technology*, 56, 9613-9622, doi:<https://doi.org/10.1021/acs.est.2c00785>, 2022.

Latham, T. L. and Nenes, A.: Water Vapor Depletion in the DMT Continuous-Flow CCN Chamber: Effects on Supersaturation and Droplet Growth, *Aerosol Sci Tech*, 45, 604-615, doi:<https://doi.org/10.1080/02786826.2010.551146>, 2011.

Meng, J. W., Yeung, M. C., Li, Y. J., Lee, B. Y. L., and Chan, C. K.: Size-resolved cloud condensation nuclei (CCN) activity and closure analysis at the HKUST Supersite in Hong Kong, *Atmos. Chem. Phys.*, 14, 10267-10282, doi:<https://doi.org/10.5194/acp-14-10267-2014>, 2014.

Sarangi, B., Ramachandran, S., Rajesh, T. A., and Dhaker, V. K.: Black carbon linked aerosol hygroscopic growth: Size and mixing state are crucial, *Atmos Environ.*, 200, 110-118, doi:<https://doi.org/https://doi.org/10.1016/j.atmosenv.2018.12.001>, 2019.

Sun, C., Zhang, Y., Liang, B., Gao, M., Sun, X., Li, F., Ni, X., Sun, Q., Ou, H., Chen, D., Zhou, S., and Zhao, J.: Morphological and optical properties of carbonaceous aerosol particles from ship emissions and biomass burning during a summer cruise measurement in the South China Sea, *Atmos. Chem. Phys.*, 24, 3043-3063, doi:<https://doi.org/10.5194/acp-24-3043-2024>, 2024.

1065

1066 Figure 8. The normalized mean bias (NMB) calculated by “Internal-mixed” scheme and “External-  
 1067 mixed” scheme according to CCN closure method. The marker of circle means “Internal-mixed”  
 1068 scheme and the marker of triangle means “External-mixed” scheme. Different colors means different  
 1069 supersaturations.

1070